On the origin of seismic anisotropy in the shallow crust of the Northern Volcanic Zone, Iceland

Conor Andrew Bacon[1], Jessica Johnson[2], Robert Stephen White[3], and Nicholas Rawlinson[1]

[1]University of Cambridge
[2]University of East Anglia
[3]Bullard Laboratories

November 24, 2022

Abstract

The Icelandic crust is a product of its unique tectonic setting, where the interaction of an ascending mantle plume and the mid-Atlantic Ridge has caused elevated mantle melting, which has accreted and cooled in the crust to form an oceanic plateau. Here, we investigate the strength, orientation and distribution of seismic anisotropy in the upper crust of the Northern Volcanic Zone using local earthquake shear wave splitting, with a view to understanding how the contemporary stress field may influence sub-wavelength structure and processes. This is achieved using a dataset comprising >50,000 earthquakes located in the top 10 km of the crust, recorded by up to 70 stations over a 9 year period. We find that anisotropy is largely confined to the top 3–4 km of the crust, with an average delay time of 0.10 ± 0.08 s and an average orientation of the fast axis of anisotropy of N15° ± 33°E, which closely matches the spreading direction of the Eurasian and North American plates (˜N16°E). These results are consistent with the presence of rift-parallel cracks that gradually close with depth, the preferential opening of which is controlled by the regional stress field. Lateral variations in the strength of shear wave anisotropy reveal that regions with the highest concentrations of earthquakes have the highest SWA values (˜10%), which reflects the presence of significant brittle deformation. Disruption of the orientation of the fast axis of anisotropy around Askja volcano can be related to local stress changes caused by underlying magmatic processes.

On the origin of seismic anisotropy in the shallow crust of the Northern Volcanic Zone, Iceland

C. A. Bacon[1], J. Johnson[2], R. S. White[1], N. Rawlinson[1]

[1]Department of Earth Sciences, University of Cambridge, UK
[2]School of Environmental Sciences, University of East Anglia, UK

Key Points:

- Anisotropy is caused by fracturing of brittle crust to a depth of 3–4 km.
- Orientation of the fast axis of anisotropy is rift parallel, and hence controlled by regional stresses.
- Disruption of anisotropy pattern around Askja volcano likely caused by magmatic intrusion and solidification.

Corresponding author: C. A. Bacon, `conor.bacon@cantab.net`

Abstract

The Icelandic crust is a product of its unique tectonic setting, where the interaction of an ascending mantle plume and the mid-Atlantic Ridge has caused elevated mantle melting, which has accreted and cooled in the crust to form an oceanic plateau. Here, we investigate the strength, orientation and distribution of seismic anisotropy in the upper crust of the Northern Volcanic Zone using local earthquake shear-wave splitting, with a view to understanding how the contemporary stress field may influence sub-wavelength structure and processes. This is achieved using a dataset comprising >50,000 earthquakes located in the top 10 km of the crust, recorded by up to 70 stations over a 9 year period. We find that anisotropy is largely confined to the top 3–4 km of the crust, with an average delay time of $0.10 \pm 0.08s$, and an average orientation of the fast axis of anisotropy of N15°±33°E, which closely matches the spreading direction of the Eurasian and North American plates (∼ N16°E). These results are consistent with the presence of rift-parallel cracks that gradually close with depth, the preferential opening of which is controlled by the regional stress field. Lateral variations in the strength of shear wave anisotropy reveal that regions with the highest concentrations of earthquakes have the highest SWA values (∼10%), which reflects the presence of significant brittle deformation. Disruption of the orientation of the fast axis of anisotropy around Askja volcano can be related to local stress changes caused by underlying magmatic processes.

Plain Language Summary

Iceland is well known for its earthquakes and volcanoes, which have helped to produce an awe-inspiring primordial landscape over the last 20 million years or so. The emergence of Iceland in the North Atlantic ocean can be attributed to the interaction of the mid-Atlantic Ridge, where new oceanic crust is formed between the North American and Eurasian plates, and a rising conduit of hot mantle from deep in the Earth, known as a mantle plume. The confluence of these two phenomenon has produced excessive melting of mantle rocks, which has accreted and cooled to form the Icelandic crust. In this study, we investigate how extensional stresses related to the divergence of the two tectonic plates has influenced the upper 3–4 km of the crust in the Northern Volcanic Zone in the deep interior of Iceland. To do so, we exploit information contained in recordings of earthquakes from the neighbourhood of Askja volcano, which suggests that rift parallel cracks that gradually close with depth permeate the upper crust. This relationship between the regional stress field associated with rifting and brittle deformation in the uppermost crust breaks down around Askja volcano itself, where magmatic processes likely cause local changes in stress field.

1 Introduction

Iceland lies in the North Atlantic, at the confluence of the divergent plate boundary (defined by the mid-Atlantic Ridge) between the Eurasian and North American plates, and the Iceland plume (White & McKenzie, 1995). Through a combination of increased melt volumes (Maclennan et al., 2001) and dynamic support from the plume, Iceland has emerged from beneath the North Atlantic and steadily grown over the last 20 million years. The resultant oceanic crust is unusually thick, reaching up to 40 km (Allen, 2002; Darbyshire et al., 2000) beneath the main glacier, Vatnajökull. On land, the mid-Atlantic Ridge is expressed as a collection of en-échelon axial rift systems, each typically comprising a central volcano and an elongated fissure swarm (Einarsson, 1991), and formally classified based on the surface fractures, faults and geochemistry of the erupted products. This neo-volcanic zone is broadly divided into three significant segments: the Western, Eastern, and Northern Volcanic Zones (WVZ, EVZ, and NVZ, respectively —Figure 1a). The Northern and Eastern zones have been offset by over 100 km from the mid-Atlantic Ridge by a series of eastward ridge jumps around 8–8.5 Ma (Garcia et al., 2003). The NVZ is subdivided into five distinct, mature volcanic systems, namely: Kverkfjöll, Askja, Fremrinámur, Krafla, and Þeistareykir. It is within these volcanic rift zones that plate spreading is accommodated through faulting and episodic accretion of new crust in volcanic intrusions and eruptions (e.g. Sigmundsson et al., 2014).

Askja is a large, active central volcano located at the southern end of the NVZ (see Figure 1). A complex, nested sequence of at least three caldera, spanning 20 km, constitutes the main volcanic edifice, which is composed primarily of hyaloclastite and pillow lavas erupted during the last glacial maximum. The last eruption of Askja was in 1961, when a 2 km-long fissure opened up, with lava breaching the eastern side of the main caldera wall. Surface mapping around Askja has revealed a complex pattern of both caldera-concentric and rift-parallel features (Graettinger et al., 2019; Hjartardóttir et al., 2016).

Deformation around Askja has been monitored since 1961, at first with a tilt line within the caldera (Sturkell et al., 2006; Tryggvason, 1989), but more recently using satellite-based GPS and InSAR measurements (de Zeeuw-van Dalfsen et al., 2012; Pagli et al., 2006; Sturkell et al., 2006). The long term trend since 1961 is one of deflation, albeit at a decaying rate. Forward modeling of the geodetic observations has lead to the possible discovery of a shallow (3.5 km), Mogi-type source beneath the Askja caldera that best fits the observed deflation, though most studies have assumed an isotropic, elastic half-space, which may be inappropriate around Askja (Drouin et al., 2017; Heimisson & Segall,

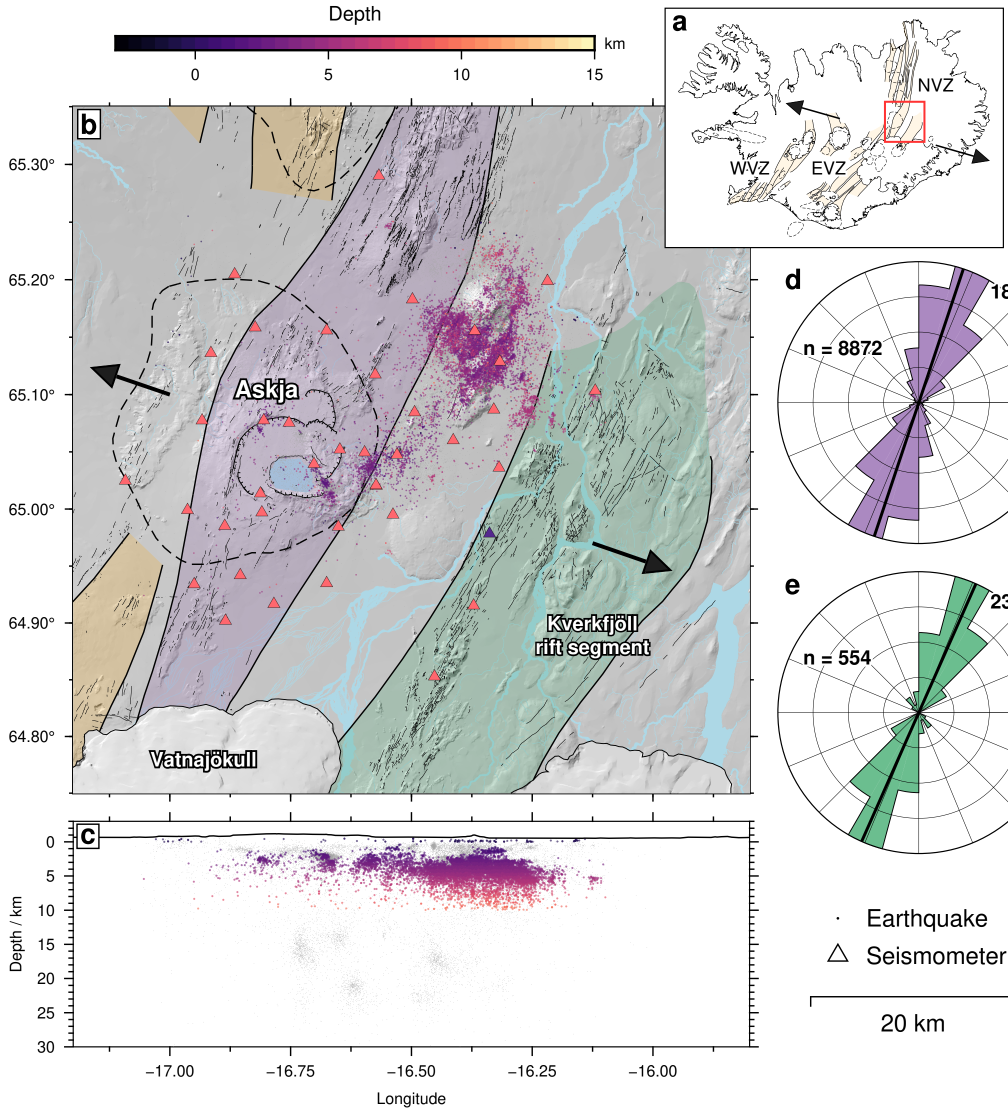

Figure 1. (a) Overview of Iceland with the major glaciers outlined. The orange bands delineate the en-echelon fissure swarms that characterise the on-land expression of the northern mid-Atlantic Ridge. The study region shown in panel (b) is outlined in red. (b) Shaded digital elevation map for the region around Askja volcano. Red triangles are seismic stations operated by the University of Cambridge used in this study. The purple triangle is the Icelandic Meteorological Office station, MKO. The entire earthquake catalog of Greenfield et al. (2018) is shown as grey dots, with those colored by hypocentral depth representing earthquakes used in this study. Two fissure swarms are highlighted: Askja's (purple) and Kverkfjöll's (green). The dashed line delineates the region associated with the Askja central volcano. The arrows show the regional direction of plate spreading, striking at N106°E (c) An east-west section showing the earthquake catalog locations. (d) and (e) are polar histograms of surface features (fractures, fissures, faults) mapped by Hjartardóttir et al. (2016) for the Askja and Kverkfjöll fissure swarms, respectively, with average strikes of 18.4° and 23.9° shown by the black bars. n is the number of features in each sample.

2020). For instance, rheological models based on a visco-elastic ridge appear to be key in the interpretation of geodetic data (Pedersen et al., 2009).

Large systems of fissures and faults are widespread across the rift segments associated with Askja and another central volcano, Kverkfjöll, situated to the southeast (see Figure 1). A network of cross-cutting faults are thought to accommodate the strain due to relative extension between these two segments (Green et al., 2014), though elsewhere the areas between the rift segments are relatively aseismic, suggesting they experience lower stress. These faults are responsible for the bulk of the seismic activity in the southern NVZ. This seismicity tends to occur in swarms (where the earthquakes are clustered in both space and time), located primarily above the well-mapped brittle-ductile transition at around 8 km depth (Soosalu et al., 2010). There is also significant seismic activity in the Öskjuvatn caldera, which lies within Askja, associated with the migration of geothermally heated fluid, as well as a number of deep clusters of earthquakes thought to be associated with the migration of melt between layered sills (Greenfield et al., 2018).

Seismic anisotropy, the directional dependence of seismic wave-speed, has been observed in the crust across a range of environments (Boness & Zoback, 2006; Johnson et al., 2011; Illsley-Kemp et al., 2018). The nature of anisotropy can, broadly, be described as either effective, i.e. a long-wavelength, bulk property of an otherwise heterogeneous medium, or intrinsic anisotropy, arising from the anisotropic elastic structure at the crystal lattice level. The latter, commonly known as Lattice Preferred Orientation (LPO), is often invoked to explain observations of anisotropy in the upper mantle, which is predominantly composed of the anisotropic minerals olivine and orthopyroxene. When deformed under strain, these minerals preferentially align, giving rise to anisotropy on a macroscopic scale. It has also been proposed as a mechanism to explain observations of Love and Rayleigh wave anisotropy in the lower crust of Iceland from ambient noise analysis (Volk et al., 2021). However, it is effective anisotropy that is typically invoked as the primary mechanism behind seismic anisotropy in the shallow, brittle crust. Here, mechanisms are typically related to either stress, through preferential closure of micro-cracks (or Extensive Dilatancy Anisotropy, EDA Crampin, 1994), oriented melt pockets (OMP; Holtzman et al., 2003; Keir et al., 2005; Bastow et al., 2010), structure, such as repeating isotropic layers (Backus, 1962) or damage zones around faults (Boness & Zoback, 2006). We seek here to determine the mechanism, or mechanisms, responsible for generating seismic anisotropy in the crust around Askja in order to better understand the state and structure of nascent crust formed at a mid-ocean ridge. Mapping and understanding this regional anisotropy is key to studying how the crust responds to transient stress changes, such as those induced by volcanic intrusions and eruptions.

Shear-wave splitting is one of the most unambiguous indicators of seismic anisotropy. When a linearly polarised shear wave impinges on an anisotropic medium, it is partitioned into two quasi-S waves, which propagate with different wavespeeds. The polarisation of these two waves, commonly called 'fast' (denoted ϕ hereafter) and 'slow', is determined by the symmetry and orientation of the anisotropic elastic tensor. A time lag, δt, accrues between the polarised waves as they propagate through the region, with the final integrated value proportional to both the path length and the strength of anisotropy. Significant work has been done to establish methods that can distinguish between structural and stress-induced anisotropy (Johnson et al., 2011; Boness & Zoback, 2006), since being able to do so is critical for the application of time-series analysis to shear-wave splitting observations as a means of monitoring the evolution of the stress field in volcanic environments in response to seasonal signals, long-term temporal signals (such as deflation and inflation), and stress transients resulting from volcanic processes such as caldera collapse and dike intrusions. In both structural and stress-induced anisotropy, the fracture density and fracture aspect ratio are among some of the dominant controls on the amount of splitting accumulated along the raypath.

Here we perform local earthquake shear-wave splitting analysis in the neighbourhood of the volcano Askja for the first time, in order to relate observed anisotropy to the underlying processes responsible for the accretion of new crust at a mid-ocean ridge and the development of associated volcanic systems. The results provide a new perspective on a region that is already well studied using complementary geophysical methods (Sturkell et al., 2006; de Zeeuw-van Dalfsen et al., 2012; Greenfield et al., 2016, 2018; Drouin et al., 2017).

2 Data and Methods

2.1 Data

We use continuous seismic data recorded by a network of 3-component seismometers operated by the University of Cambridge since 2008, with additional data from one instrument operated by the Icelandic Meteorological Office (MKO, denoted by the purple triangle in Figure 1). Over time, the network has consisted of between 30 and 70 broadband instruments, primarily Güralp 6TDs (30 s corner frequency). All data used in this study were recorded using Güralp 6TDs. For the shear-wave splitting analysis, we use the earthquake catalog of Greenfield et al. (2018) which spans 2009-2015, updated (using the same methodology outlined in their paper) to include data recorded between 2015 and 2018 (Winder et al., 2018). These earthquakes were detected and located using the automatic Coalescence Microseismic Mapping algorithm (CMM: Drew et al., 2013). The details of pre-processing applied to the data to generate this catalog is available in Greenfield et al. (2018). The CMM algorithm produces automatic arrival time picks for P- and S-phases that were used, along with some manually picked phase arrivals, to relocate the events using NonLinLoc (Lomax et al., 2000). The final catalog consists of 58,143 individual earthquakes spanning a local magnitude range of -0.6–4.0, with a magnitude of completeness of ≈ 1.

The majority of earthquakes (52,141, or 89.7%) occur in the brittle, upper 7 km of crust, generated primarily by a network of cross-cutting conjugate strike-slip faults oriented N-S and SW-NE, located to the northeast of Askja volcano and to the south of Herðubreið, a tuya formed during the last glacial period (Figure 1a). These faults accommodate tectonic stresses that are concentrated by the relative spreading between the Askja and Kverkfjöll rift segments. The remaining shallow seismicity is related to geothermal processes at Askja volcano. The depths of these shallow events are well-distributed throughout the brittle crust. The final 10.3% (6,002) of events in the catalog occur in pockets at depths between 7 and 25 km in the typically aseismic lower, ductile crust. These are thought to be associated with magmatic processes (Greenfield et al., 2018; Martens & White, 2013). We limit our analyses to splitting observed from earthquakes originating in the upper 10 km of crust in order to specifically focus on anisotropy in the shallow crust. Finally, we exclude any events that occurred between August 2014 and February 2015 in order to remove the possible effect of stress transients related to the 2014–15 eruption of Bárðarbunga. Figure 1 illustrates the spatial distribution of earthquakes and seismic stations between 2009 and 2018 that have been used in this study.

2.2 Shear-wave splitting

We measure the shear-wave splitting parameters $(\phi, \delta t)$ using the Multiple Filter Automatic Splitting Technique package (MFAST version 2.2 Savage et al., 2010; Teanby et al., 2004), which uses the eigenvalue minimisation algorithm of Silver and Chan (1991). Figure 2 illustrates the process for a good quality event; further examples can be found in the Supplementary information (see Figures S1-4). Unlike other methods, this does not require any knowledge of the initial polarisation, though at the cost of being more prone to cycle skipping. A grid search over δt and ϕ is used to find the pair of values that best remove the observed splitting, determined by measuring the linearity of particle motion on the horizontal components within a window around the S-phase arrival. This is further automated by trialing multiple windows and using cluster analysis to identify stable results. Errors for individual measurements are calculated by conducting an F-test and finding the 95% confidence interval on the optimal $(\delta t, \phi)$ (Walsh et al., 2013). Each measurement is automatically graded based on the distribution of clusters and the tightness of the misfit contours from the grid search (Savage et al., 2010). Also, MFAST trials a suite of filters over the S-phase pick in order to determine the filter that most effectively boosts the signal-to-noise ratio. Table S1 in the supporting information provides an overview of the final parameters used for MFAST.

We limit our analyses to the subset of measurements that satisfy the following criteria: a signal-to-noise ratio (as defined in Savage et al., 2010) greater than 4; clusters graded “ACl” (a measure of the number of clusters identified and how tight they are); errors in $\phi < 10°$ in order to mitigate erroneous observations resulting from cycle skipping; values of $\delta t < 0.48s$, equal to 0.8 times the maximum delay time of the search; and errors in $\delta t < 0.05s$ as an additional filter against ‘null’ measurements and poorly constrained results. A null measurement can occur when there is no anisotropy in the plane of the shear wave particle motion, or when the source polarisation of the shear wave is along the fast or slow orientation of the medium. Source polarisations are determined from the uncorrected horizontal particle motion. Measurements of ϕ within 20° of the source polarisation are considered too ambiguous in that they cannot be definitively distinguished from nulls. After applying these criteria, we are left with over 100,000 measurements of shear-wave splitting. Finally, we further remove measurements for which the angle of incidence of the shear wave at the surface falls outside the shear-wave window (Nuttli, 1961). This window, defined by $\sin^{-1}(V_s/V_p)$, is the angle to the vertical at which there will be non-negligible interactions with the free surface that would alter the phase and amplitude information on the horizontal components (Crampin, 1984). A V_p/V_s ratio of 1.78 corresponds to a shear-wave window of $\sim 34°$ from the vertical. However, volcanic environments typically exhibit very low velocities in the topmost layers (Lesage et al., 2018), which will cause significant deflection of the ray towards the vertical. Therefore, we limit our analysis to event-station pairs with a straight-line angle-of-incidence at the surface of $< 50°$. This leaves over 16,000 high-quality measurements of shear-wave splitting.

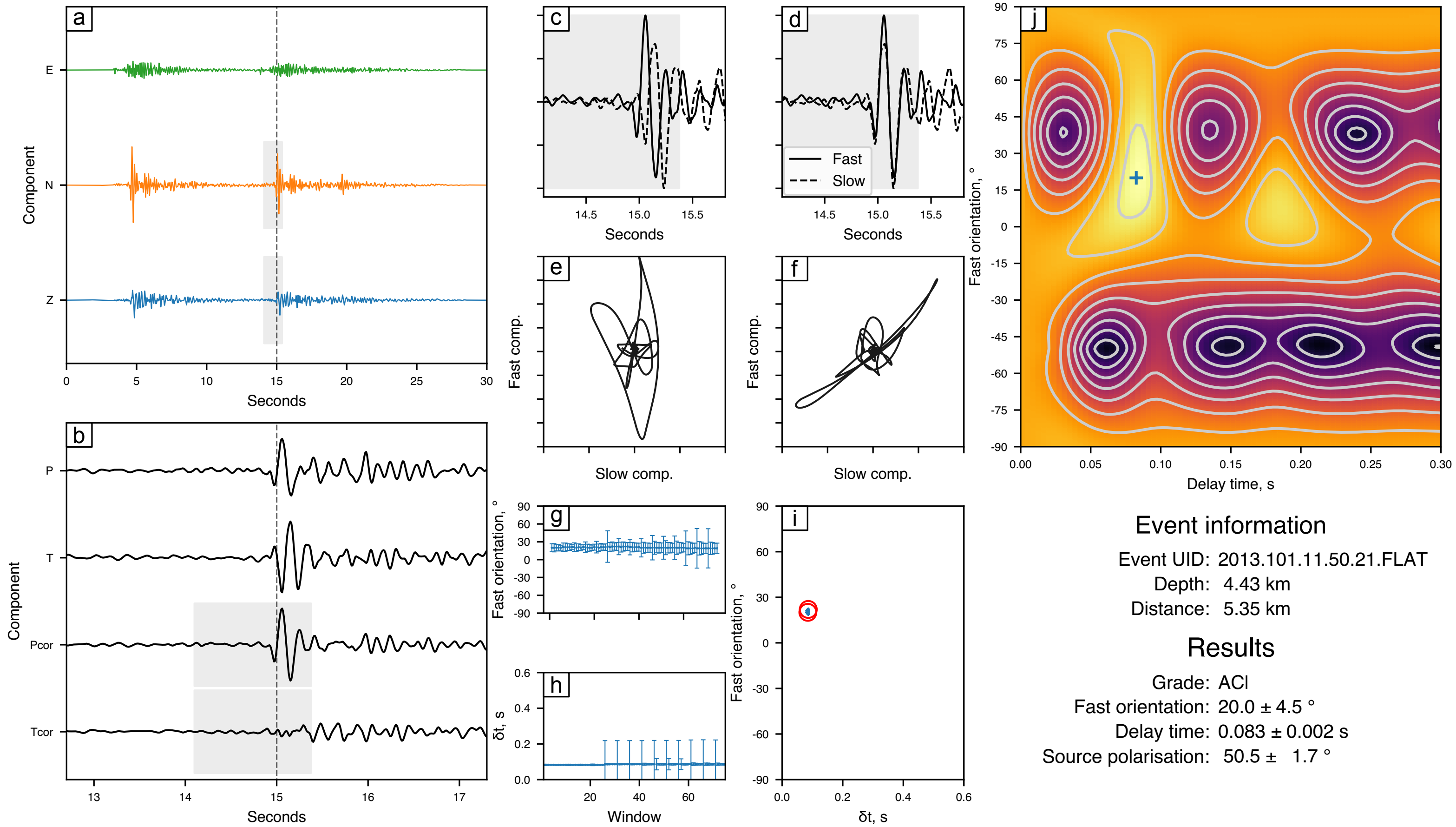

Figure 2. An example of a good splitting measurement. (a) shows the raw data for the East (green), North (orange), and Vertical (blue) components. (b) shows a zoom in around the S phase arrival rotated onto the nominal 'radial' (P) and 'transverse' (T) axes before and after correction for splitting. (c) and (d) show the phase arrivals rotated onto the 'fast' and 'slow' axes before and after correction, with (e) and (f) showing the corresponding particle motion. There is a clear linearisation of the particle motion of the horizontal components and removal of energy from the transverse component. Panels (g) - (i) show the results of the multiple window trials and the cluster analysis. Finally, (j) shows the resultant grid of the minimised eigenvalue. The blue cross denotes the optimal (δt, ϕ) pair.

2.3 Shear Wave Anisotropy

The delay time is an integrated measure of the strength of anisotropy along the raypath, making it unsuitable for direct comparison between different event-station pairs. Instead, the observed delay times are converted to shear wave anisotropy (SWA: Thomas & Kendall, 2002), which is a measure of the strength of anisotropy as defined by the fractional perturbation, a, from the average shear wave speed, $\bar{v}$:

$$\begin{aligned}\delta t = t_{slow} - t_{fast} &= \frac{d}{v - \frac{1}{2}av} - \frac{d}{v + \frac{1}{2}av} \\ \Rightarrow a &= \frac{-2d}{\delta t \bar{v}} \pm \sqrt{4 + \left(\frac{2d}{\delta t \bar{v}}\right)^2}\end{aligned} \tag{1}$$

where t_{slow} and t_{fast} are the slow and fast traveltimes, respectively. SWA is normalised against the path length, d, of the ray, therefore representing a more appropriate metric to compare between individual observations. We assume straight-line raypaths and use an optimal 1-D velocity model determined by inverting microseismic arrival times (Mitchell et al., 2013). Nowacki et al. (2018) demonstrates that the errors introduced by the straight-line raypath assumption is negligible for shallow events, for which the raypaths do not deviate far from a straight line, with up to around 1% overestimation in SWA for the deepest events. Additionally, they show that the uncertainty in SWA arising from inaccuracy in the velocity model is estimated to be less than 1% from bootstrap modeling. Given the similarities between the regions of study (Iceland and the Afar), we believe that this uncertainty analysis remains appropriate.

3 Results

3.1 Regional averages

3.1.1 Delay times

From the entire catalog of shear-wave splitting measurements, we recover an average delay time of $\delta t = 0.10 \pm 0.08$ s. This value is consistent with similar datasets, e.g. ∼0.2 s around Soufrière Hills volcano, Montserrat (Baird et al., 2015); 0.1–0.2 s in the Western Volcanic Zone, Iceland (Menke et al., 1994); and 0.11 ± 0.06 s around Aluto volcano, Ethiopia (Nowacki et al., 2018). We find the distribution of delay time observations to be sufficiently normal, justifying the extraction of a regional 1-D depth profile as the central tendency of the data via the application of a rolling arithmetic mean (Figure 3). We use a 1.5 km rolling window, spaced every 0.75 km, which is controlled by the uncertainty in hypocentral depth for shallow events. We observe a constant delay time at depths $>$ 3 km. Between 3 km depth and the surface, the delay time begins to trend towards 0, which is consistent with a finite-thickness anisotropic layer in the very shallow crust, a common observation across volcanic environments (Johnson et al., 2011; Menke et al., 1994; Nowacki et al., 2018). This does not preclude structural control on anisotropy, but it is a key requirement for stress-induced anisotropy due to the preferential closure of microcracks. In oceanic-type crust, most pore space has been closed by lithostatic pressure at around 4–5 km below the surface (Christensen, 1984). The relationship between crustal porosity and depth can be expressed as the exponential function (e.g. Athy, 1930; Audet & McConnell, 1992):

$$\Phi(r) = \Phi_1 exp\left(\frac{-c * P(r)}{P_c}\right) \tag{2}$$

where c is a constant (~ 6.15), Φ_1 is the surface porosity, $P(r)$ is the lithostatic overburden pressure ($= \rho(r)gd$, where ρ is the density, g is the acceleration due to gravity, and d is the depth), and P_c is the characteristic closing pressure of the material (Han et al., 2014). We perform a simple fit of a similar exponential function to the depth profile, shown in Figure 3, which suggests that the 1-D behaviour of the delay time is consistent with the presence of crustal cracks that gradually close with increasing depth.

3.1.2 Fast axis orientation

We observe an average orientation of ϕ ~N15°E±33° for the fast axis of anisotropy, though we recommend caution in drawing too much from the exact value of, and the uncertainty on, this measure as the circular statistics used are only appropriate if the observations are drawn from a unimodal distribution. Small variations in fast polarizations across the region, such as those expected in response to e.g. a rotation in the stress field, may be contributing to the large spread in observed ϕ values. The average orientation correlates well with the normal to the plate-spreading direction, as shown in Figure 4, which is consistent with observations made at other spreading centres, such as the northern Main Ethiopian Rift (Keir et al., 2005). Exactly how the orientation of the fast axis of anisotropy varies across the region is investigated further in Section 3.2.2.

3.2 Lateral variations in observed anisotropy

3.2.1 Shear wave anisotropy

Measurements of delay time are converted to SWA using equation 1, as described in section 2.3. We constrain the shallow anisotropic layer to be entirely above ~3 km b.s.l., inferred from the constant delay time below this depth observed in the 1-D profile (Figure 3). Assuming that the mechanism generating seismic anisotropy is aligned fractures in the shallow crust, this value is consistent with measures of fracture density

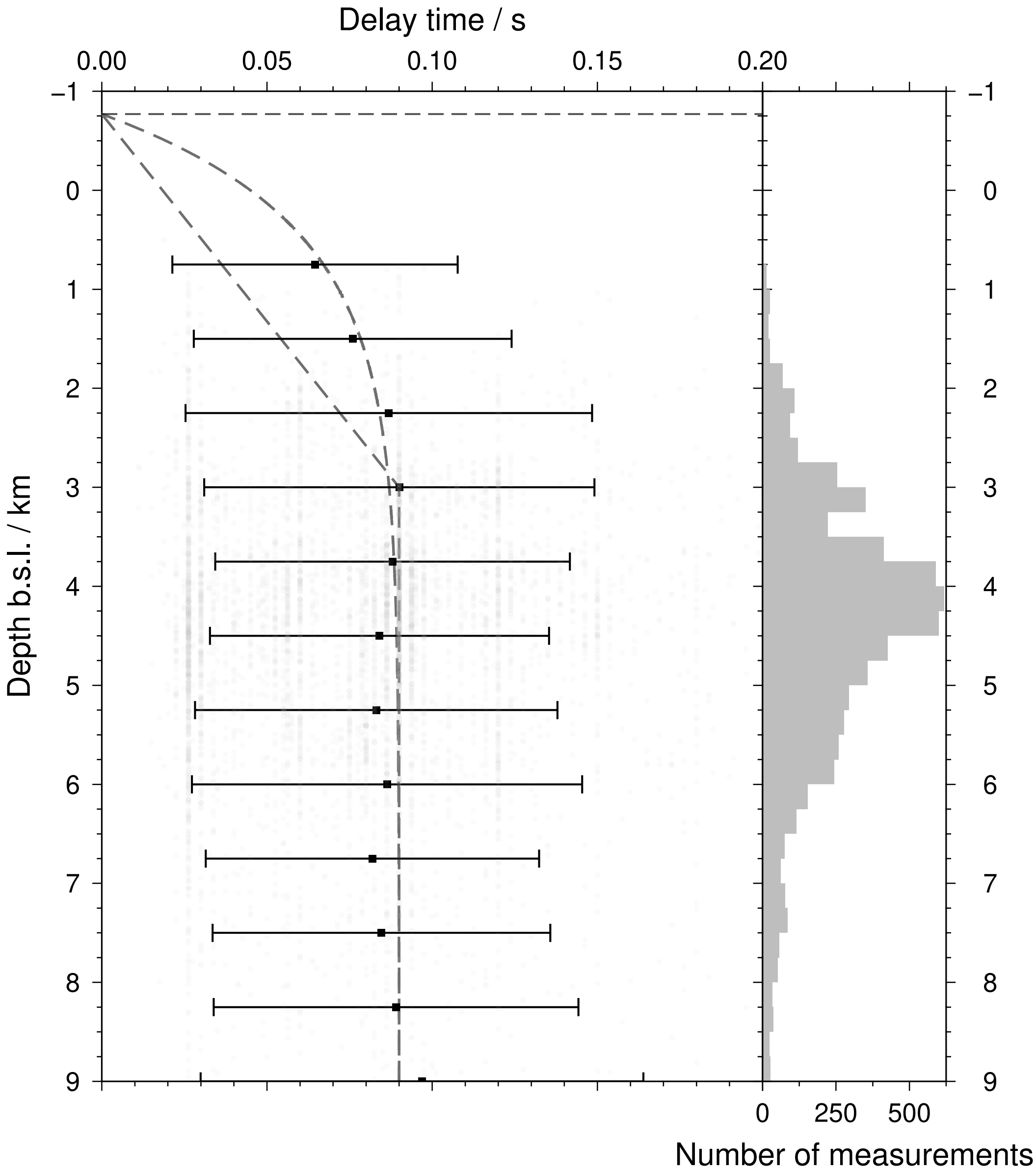

Figure 3. 1-D depth profile of delay time from a 1.5 km wide rolling window, spaced every 0.75 km. The dashed lines show the expected trends for a finite-thickness anisotropic layer down to 3 km depth with a strength of 3.4% and an exponential model based on the reduction of porosity as a function of depth. Black squares show the measured arithmetic means for each bin, with the associated one standard deviation of uncertainty shown by the error bars.

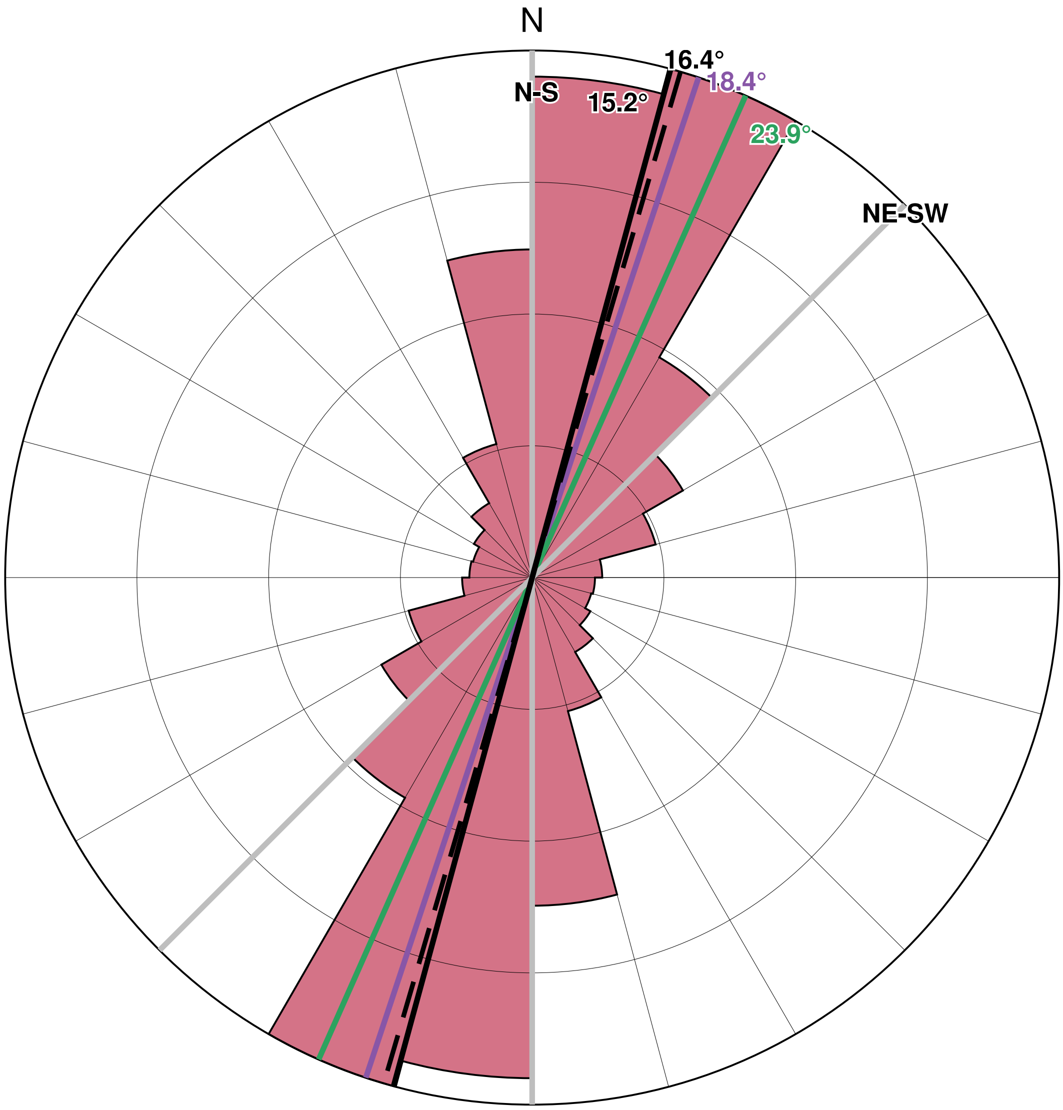

Figure 4. Circular histogram of all fast orientation measurements as denoted by pink shading. Lines are used to show the average strikes of the cross-cutting, conjugate strike-slip faults (grey), the average strikes of surface features in the Askja and Kverkfjöll rift segments (purple and green, respectively), the direction normal to spreading (dashed black), and the overall average orientation of the fast axis of anisotropy (black). There is a very strong correlation between the fast orientation direction and the direction normal to spreading, suggesting that stress is the dominant control on anisotropy.

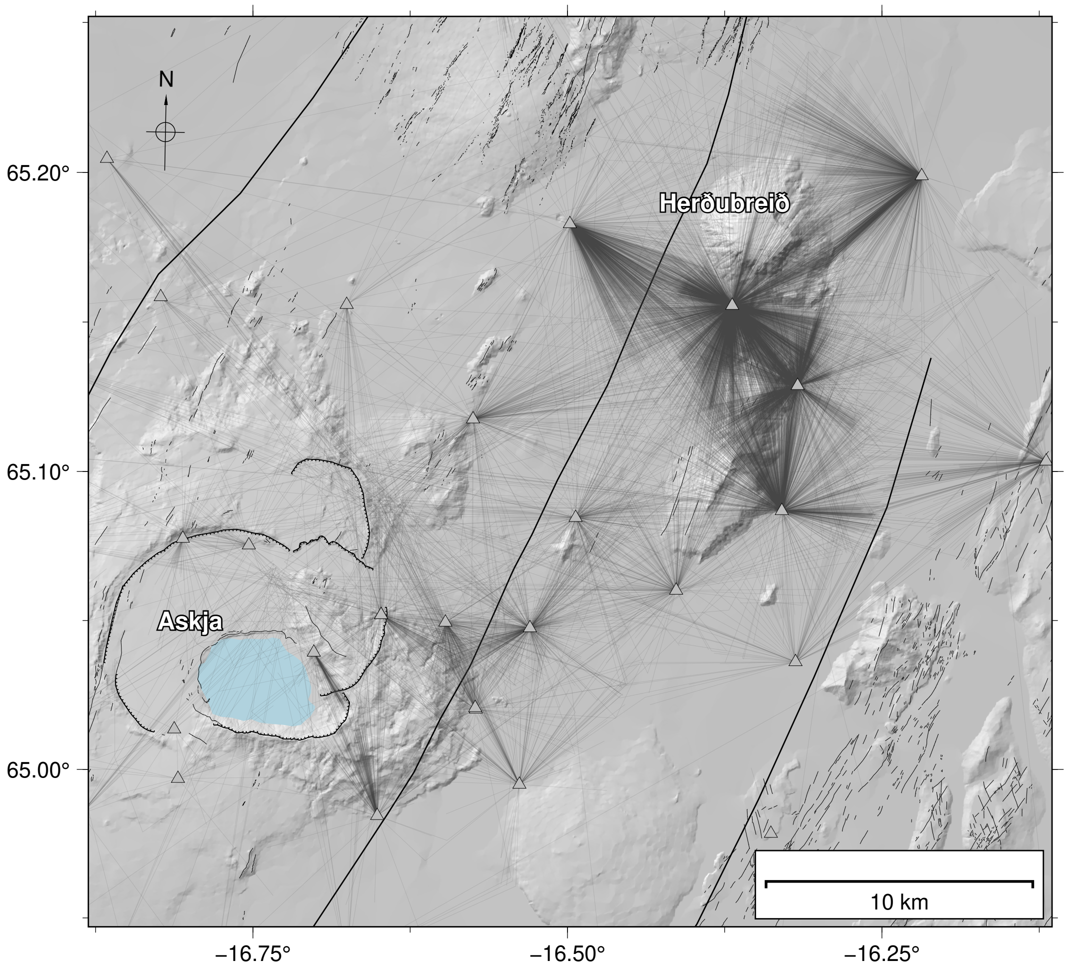

Figure 5. Map showing the raypath coverage for the study region. There is very good coverage around Askja and in the inter-rift segment around Herðubreið. The black lines depicting the raypaths are plotted at 85% transparency.

from other independent measures, such as ambient noise dispersion curves (Volk et al., 2021), response to seasonal changes in load in dv/v (Donaldson et al., 2019), and general profiles of pore space as a function of depth in oceanic crust (e.g. Carlson & Herrick, 1990). While there is an element of bias in assigning the splitting observation to a single point in space, we follow precedent and use the mid-point of the raypath (Figure 5) between the source and receiver before re-gridding the data. For near-vertical raypaths, as is the case for the majority of our dataset due to the shear-wave window constraint, this introduces negligible systematic error in the pattern of lateral variations. The application of a symmetric 2-D Gaussian spatial filter to the re-gridded observations further reduces the impact of this assumption on the observed lateral patterns. Here we present the results for a grid with 0.5 x 0.5 km cells and a minimum observation count of 10, and 2-D Gaussian spatial filter with a half-width of 1 km (Figure 6). The key features of the lateral variation in anisotropy strength are robust to perturbations to both the grid parameters and the smoothing radius. We trialed cell sizes varying from 0.25 x 0.25 km^2 – 1 x 1 km^2, minimum number of observations per bin between 3 and 15, and a smoothing radius of 1–3 km, and found that the results did not vary significantly (see supplementary Figure S1). We acknowledge that the process of re-gridding the data in this way means that some azimuthal information is lost, but we deem it acceptable for the purpose of identifying trends in the strength of anisotropy across the rift segment. We measure an anisotropic strength of $\sim$5%, with values ranging between 2–12 %, which spans the appropriate range expected for mechanisms proposed for elastic anisotropy of the crust.

3.2.2 Fast axis orientation

We re-grid the observations of ϕ by grouping them laterally by the midpoint along the event-receiver raypath (Figure 5), with the results presented in Figure 7. We use an adaptive quad-tree gridding method, which allows us to increase the detail (down to a minimum cell size of 2 x 2 km^2) where we have a higher density of observations. The minimum cell size used is on the same order as the uncertainties in the epicentral locations for the earthquakes in the catalog. Starting from a single cell spanning the entire study region, this process recursively subdivides a cell into four sub-cells if the number of observations in the cell exceeds 200. Any cells with fewer than 50 observations are omitted from the final grid. Within each cell, the resultant vector is evaluated from which both the average orientation and the *mean resultant length*, $\hat{R}$, is determined. $\hat{R}$ is a measure of dispersion analogous to the variance (in the opposite sense) - values close to 0 imply near uniform dispersion, whereas values close to 1 suggest that the orientations are tightly bunched around a particular value (e.g. Davis & Sampson, 1973). This al-

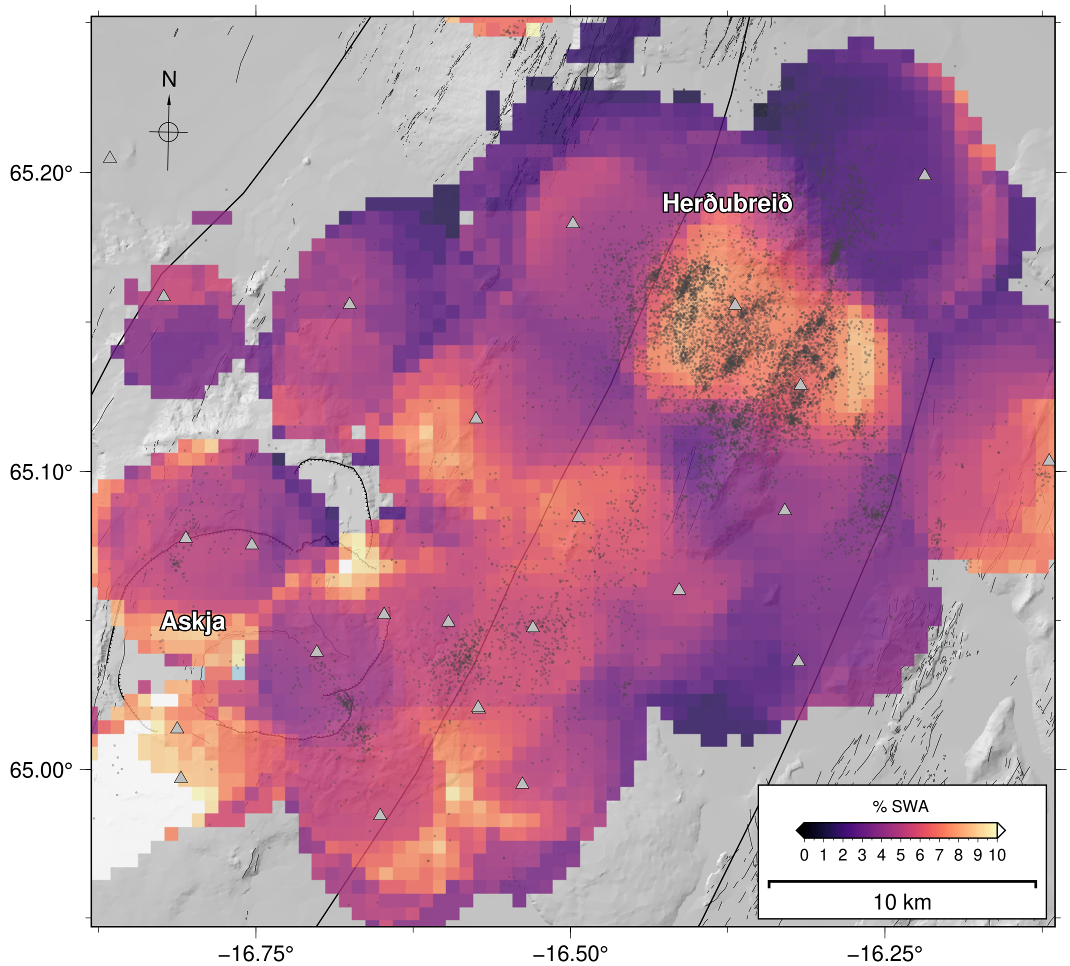

Figure 6. Map of the lateral variation in percentage shear wave anisotropy from earthquakes shallower than 10 km (denoted by the small black dots). Stations from which data have been used are denoted by the grey triangles.

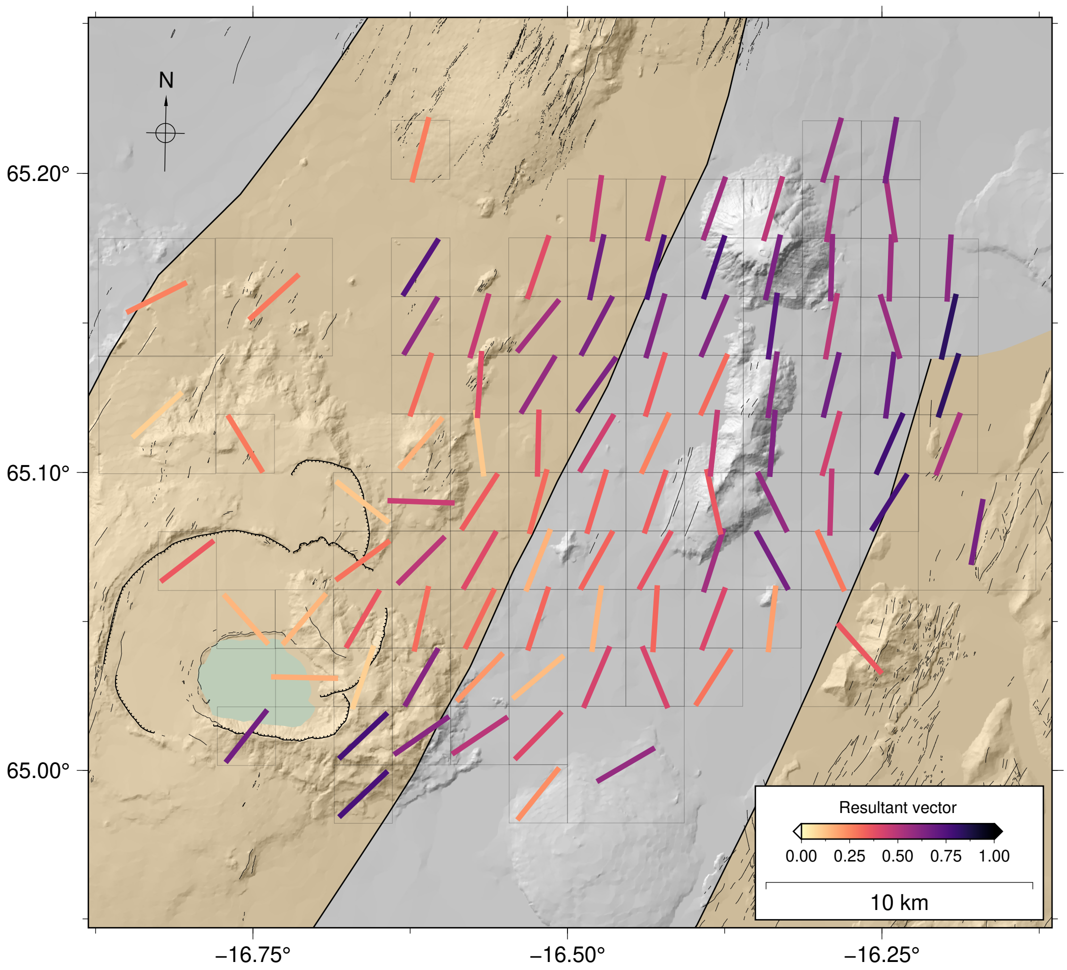

Figure 7. Lateral variations in observed fast axis orientations, ϕ. The observations have been assigned to the midpoint between source and receiver, then re-gridded using a quadtree method. The resultant grid is plotted using faint black lines. Within each cell, the bar represents the average fast orientation, colored by the 'resultant vector' which is a measure of dispersion/coherence of the orientation data. Darker colors indicate stronger coherence.

lows us to observe trends in the orientation of anisotropy, without constraining the source of anisotropy to be in the vicinity of the source or the receiver.

4 Discussion

4.1 Anisotropy orientation and strength

Our analysis of shear-wave splitting from earthquakes in the brittle, upper 10 km of crust around Askja has constrained the primary source of anisotropy to be in the top 3–4 km of crust. The dominant orientation of the fast axis of anisotropy is strongly correlated with the strike of the rift (Figure 4). Together, these two observations provide compelling evidence for extensional stress as the underlying mechanism generating the anisotropy. This is consistent with other studies of local shear-wave splitting in similar environments, such as the East African Rift (Keir et al., 2005; Nowacki et al., 2018; Illsley-Kemp et al., 2017, 2019). The average delay times of shear-wave splitting observations ($\delta t = 0.10 \pm 0.08s$) is also consistent with these studies.

Although we attribute our observations of shear wave anisotropy to fractures or cracks in the shallow crust, there are other causes of anisotropy that may be a factor. For instance, aligned melt pockets could produce a signature of effective anisotropy with ridge-parallel orientation of the fast axis, as has been suggested in the upper mantle and lower crust of the Main Ethiopian Rift (Kendall et al., 2005; Hammond et al., 2014). However, there is no evidence of this in the shallow crust beneath the NVZ, and ambient noise studies that constrain azimuthal variations of radial anisotropy are not consistent with such a mechanism (Volk et al., 2021). Furthermore, it would be unusual for melt pockets to focus in the very shallow crust, and be absent at greater depth, which would need to be the case to explain the trend shown in Figure 3. Another possibility is LPO associated with deformation, lava flows or depositional processes. Recent measurements of radial anisotropy from ambient seismic noise (Volk et al., 2021) support the presence of LPO in the crust resulting from internal deformation or flow, but this appears to be largely restricted to depths below about 15 km, and therefore is unlikely to influence our results. Lava flows can align minerals such as plagioclase and clinopyroxene (Boiron et al., 2013), but this tends to occur at very short scale lengths horizontally and in depth, and consequently are unlikely to substantially contribute to our pattern of anisotropy over what is a relatively large study area.

When interpreting the map of SWA (Figure 6), we recommend that a greater importance be placed on the relative values, as opposed to the absolute values, which can be 'tuned' by varying the thickness chosen for the anisotropic layer. We primarily see elevated values of SWA in regions with elevated rates of seismicity, which is consistent with the idea that stress is the primary control on the mechanism generating anisotropy.

There is a region of elevated SWA to the south of Herðubreið (Figure 6), which corresponds with a region of elevated seismic activity. A network of faults connects the Askja and Kverkfjöll rift segments, which are thought to accommodate the relative rates of plate-spreading. As such, it is reasonable to assume that this section of crust is heavily fractured and highly stressed, two conditions under which one would expect to see a higher anisotropic signal. This may also be an artefact of the assumption that the anisotropic layer has a uniform thickness across the region, though there is little evidence to validate this from the individual 1-D station profiles. The relative low in SWA to the northeast of Herðubreið corresponds to a region of elevated V_p/V_s observed in a tomographic study of the region (Greenfield et al., 2016), which was interpreted to be a sign of elevated fluid content. This is consistent with the suggestion from Nowacki et al. (2018) that a higher V_p/V_s may indicate that there are more fluids present, which in turn causes lower effective anisotropy, and may also explain the relatively low SWA below the Askja geothermal field, on the eastern edge of the Öskjuvatn caldera. However, we should note that elevated V_p/V_s need not necessarily imply lower anisotropy; for instance, Wang et al. (2012) made laboratory observations of cracked samples and carried out effective media modeling, which suggested that the presence of high V_p/V_s ratios is indicative of significant crack-induced anisotropy.

The spatial trends in the orientation of the fast axis of anisotropy was shown to be broadly consistent with both the observed surface features from geological mapping and the plate spreading direction (Figure 4). This is consistent with findings from other rift environments (Menke et al., 1994; Illsley-Kemp et al., 2017; Nowacki et al., 2018), where the fast axis of anisotropy was found to be aligned to the present-day minimum compressive stress i.e. rift parallel. In these studies, the source of anisotropy is attributed to aligned cracks in the top 3–4 km of the crust. Such crack alignment in the very shallow crust is also present in other tectonic environments, including fold and thrust belts. For example, de Lorenzo and Trabace (2011) investigate local earthquake shear-wave splitting using data recorded in the central Appenines, and attribute anisotropy in the top 4–5 km of the crust to fault-parallel fluid-filled crack systems.

As Figure 6 illustrates, the orientations of the fast axis of anisotropy are not uniformly rift-parallel; for instance, in the very south they have a stronger easterly component compared to those in the north. Likewise, around Aluto in the Ethiopian Rift, the orientations become more scattered. It is likely that the regional stress field in the south of our area is overprinted by the ongoing deformation that is taking place around Askja. Subsidence of the main caldera has been ongoing since 1983 (de Zeeuw-van Dalfsen et al., 2012), possibly due to the cooling and contraction of an underlying magma body, although recent micro-gravity increases may be due to magma flow into a shallow magma chamber (de Zeeuw-van Dalfsen et al., 2013). Such local stress changes and associated deformation may be responsible for scattered horizontal velocity vectors measured by GPS stations in the vicinity of Askja (Árnadóttir et al., 2009; Drouin et al., 2017); consequently, the disruption to the pattern of anisotropy around Askja is perhaps not surprising. In the next section, we use stress modeling to investigate this phenomenon further.

4.2 Stress modeling

Numerous studies have concluded that the orientation of anisotropy in the crust is generally controlled by the regional stress field and/or the alignment of structures, such as fissures and faults (Johnson et al., 2011; Illsley-Kemp et al., 2018; Savage et al., 2010). Distinguishing between stress-induced and structural anisotropy in the Northern Volcanic Zone is made somewhat more complex by the fact that the regional stress field is also the primary control on the orientation of structural features. It is observed, however, that the system of faults between the Askja and Kverkfjöll rift segments (responsible for a large proportion of the tectonic seismicity in the region) is composed of conjugate strike-slip faults oblique to the strike of the plate margin (see Figure 1). This suggests that we can rule out fabric resulting from the damage zones around faults as a mechanism generating (significant) anisotropy, based on the regional averages.

We explored the role of stress in the generation of anisotropy by modeling the regional stress field around Askja using the Coulomb v3.3 software package (Toda et al., 2011). Whereas the ductile lower crust is able to deform by continuous creep under the extensional stresses, accretion and extension of the brittle upper crust is episodic in nature. Over time, elastic strain accumulates in the brittle crust, before being released over short, intense periods of diking and extensional faulting, as seen during the 2014–15 eruption of Bárðarbunga. The brittle-ductile boundary across the NVZ sits between 6–8 km depth (Soosalu et al., 2010). We model this process using a buried dislocation, which has previously been used to model plate boundary deformation in the rift zones of Iceland (Árnadóttir et al., 2006; LaFemina et al., 2005). This model assumes that spreading below the brittle-ductile boundary is constant and equal to the full-spreading rate, represented by an opening Okada dislocation (Okada, 1992) extending from the locking depth to infinite depth. The stress singularity at the upper edge of the buried dislocation is eliminated from the model by tapering the dislocation such that the opening gradient goes to 0 at the topmost edge (Heimisson & Segall, 2020). The spreading boundary is taken to pass through Askja, striking along the rift segment at 015°N. A small component of spreading is assigned to the Kverkfjöll rift segment, though it is debatable whether any active spreading is occuring in this region. However, this inclusion does not significantly impact the result of the modeling. The ongoing deflation beneath Askja is incorporated using the best-fitting (analytical) solution from forward modeling (Drouin et al., 2017) of GPS data. This results in a point Mogi source at 3.5 km depth beneath the Askja caldera (see Figure 8), with a volumetric change of 0.0013 km^3 / year. While both of these models are highly simplified, neglecting visco-elasticity in particular, they

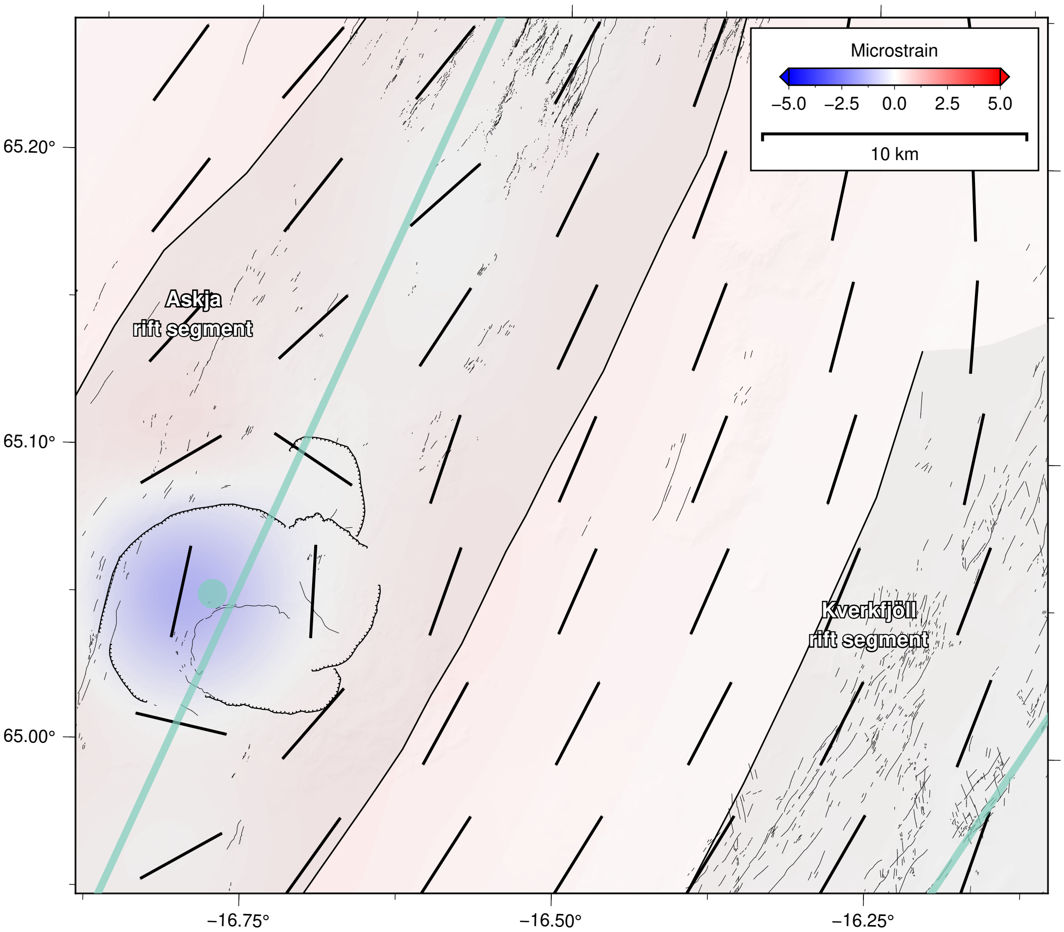

Figure 8. Modeled strain field at 0 km b.s.l. draped over a digital elevation model. Black bars represent the orientation of the maximum horizontal stress, S_{Hmax}. Blue bars delineate the modeled plate boundary segments. The blue circle denotes the centre of the observed deflation beneath Askja volcano.

are sufficient to capture, to first-order, the tectonic stress state of the crust. The input files for this modeling are available in the supporting information.

Using the method of Lund and Townend (2007), we extract the maximum horizontal stress vectors (S_{Hmax}) from the final model at a depth of 0 km b.s.l., where we expect the impact of the stress field to have the most significant effect on the opening/closure of cracks. We observe a strong correlation between the orientations of fast directions and S_{Hmax} across the region, including a similar rotation moving from south to north. This provides a strong link between the stress field and the anisotropy, as would be expected for the EDA mechanism. The differences, particularly at the southern end of the region, are likely to be due to the component of strain imparted by the presence of the Vatnajökull ice cap, which is not included in the modeling. Interpolating the strain field directly from the available GPS data may prove valuable in assessing how much of the observed rotation is due to the unmodeled components. Around Askja, the modeled strain field shows a similar level of scatter to what is observed in Figure 7, though there is no particular coherency in alignment. This is likely to be due to the limited spatial resolution of the splitting measurements, coupled with the simplifying assumptions made in the stress modeling. Careful analysis of the temporal changes in the anisotropic signal in response to stress transients, such as the 2014 Bárðarbunga-Holuhraun dike intrusion, may provide more supporting evidence for the EDA mechanism dominating the generation of anisotropy in the upper crust in the Northern Volcanic Zone.

5 Conclusions

We have presented shear-wave splitting results from the Northern Volcanic Zone, Iceland, based on a large dataset of local earthquakes that span a period of over 7 years. The dense, stable network has allowed us to image the anisotropic properties of the Icelandic crust with a high spatial resolution. These observations have allowed us to investigate the likely mechanisms generating this anisotropy, whether controlled by the stress state or structural features in the crust. The main findings of the study include (i) based on earthquakes that occur between the surface and 10 km depth, anisotropy is largely restricted to the top 3–4 km of the crust; (ii) delay time variations in the shallow anisotropic layer are consistent with the presence of cracks that gradually close with depth; (iii) SWA is strongest in regions of elevated seismicity, particularly in the zone between the Askja and Kverkfjöll rift segments, which appears to be heavily fractured; (iv) the dominant orientation of the fast axis of anisotropy is almost perpendicular to the spreading direction, which indicates that regional stress is the dominant control on anisotropy; and (v) in the neighbourhood of Askja, the orientation of the fast axis of anisotropy becomes scattered, which is consistent with stress modeling results that use a Mogi source located 3.5 km beneath the main caldera. Future work will focus on the very deep earthquakes beneath the Northern Volcanic Zone, and the constraints they may be able to supply on anisotropy in the lower crust, which has previously been imaged by ambient noise tomography.

Acknowledgments

The author contributions are as follows: **C.A.B.:** Conceptualization, Methodology, Software, Formal Analysis, Visualization, Writing - Original Draft; **J.J.:** Supervision, Writing - Review & Editing; **R.S.W.:** Supervision, Funding acquisition, Writing- Review & Editing; **N.R.:** Supervision, Funding acquisition, Writing - Review & Editing.

A number of seismometers were borrowed from the Natural Environmental Research Council (NERC) SEIS-UK facility (loans 857, 914, 968, 980, 1022 and 1115). All waveform data, except that recorded at the IMO station MKO, are available for download from the IRIS DMC. We thank the many people who participated in seismic data collection fieldwork in Iceland over the years, in particular Bryndís Brandsdóttir and Sveinbjörn Steinþórsson, without whom this work would not be possible. We also thank the Iceland Meteorological Office (IMO) for kindly providing the additional data from MKO. We especially thank Tim Greenfield and Tom Winder for their considerable efforts in producing the earthquake catalog that made this study possible. The shear-wave splitting measurements and Coulomb stress modeling input file can be downloaded from

https://doi.org/10.5281/zenodo.5007022. Data analysis was carried out using Python, with the following packages proving particularly useful: ObsPy (Beyreuther et al., 2010); SciPy (Virtanen et al., 2020); NumPy (Harris et al., 2020); Pandas (pandas development team, 2021). Data visualizations were performed using Matplotlib (Hunter, 2007) and Generic Mapping Tools (Wessel et al., 2019).

References

Allen, R. M. (2002). Plume-driven plumbing and crustal formation in Iceland. *Journal of Geophysical Research*, *107*(B8). doi: 10.1029/2001jb000584

Árnadóttir, T., Jiang, W., Feigl, K. L., Geirsson, H., & Sturkell, E. (2006). Kinematic models of plate boundary deformation in southwest Iceland derived from GPS observations. *Journal of Geophysical Research: Solid Earth*, *111*(B7). doi: 10.1029/2005JB003907

Árnadóttir, T., Lund, B., Jiang, W., Geirsson, H., Björnsson, H., Einarsson, P., & Sigurdsson, T. (2009). Glacial rebound and plate spreading: results from the first countrywide GPS observations in Iceland. *Geophysical Journal International*, *177*(2), 691–716. doi: 10.1111/j.1365-246X.2008.04059.x

Athy, L. F. (1930). Density, porosity, and compaction of sedimentary rocks. *American Association of Petroleum Geologists Bulletin*, *14*(1), 1–24. doi: 10.1306/3D93289E-16B1-11D7-8645000102C1865D

Audet, D., & McConnell, J. (1992). Forward modelling of porosity and pore pressure evolution in sedimentary basins. *Basin Research*, *4*(2), 147–162. doi: 10.1111/j.1365-2117.1992.tb00137.x

Backus, G. E. (1962). Long-wave elastic anisotropy produced by horizontal layering. *Journal of Geophysical Research*, *67*(11), 4427–4440. doi: 10.1029/jz067i011p04427

Baird, A. F., Kendall, J.-M., Sparks, R. S. J., & Baptie, B. (2015). Transtensional deformation of Montserrat revealed by shear wave splitting. *Earth and Planetary Science Letters*, *425*, 179–186.

Bastow, I. D., Pilidou, S., Kendall, J. M., & Stuart, G. W. (2010). Melt-induced seismic anisotropy and magma assisted rifting in Ethiopia: Evidence from surface waves. *Geochemistry, Geophysics, Geosystems*, *11*(6). doi: 10.1029/2010GC003036

Beyreuther, M., Barsch, R., Krischer, L., Megies, T., Behr, Y., & Wassermann, J. (2010). ObsPy: A Python toolbox for seismology. *Seismological Research Letters*, *81*(3), 530–533.

Boiron, T., Bascou, J., Camps, P., Ferré, E., Maurice, C., Guy, B., ... Launeau, P. (2013). Internal structure of basalt flows: insights from magnetic and crystallographic fabrics of the La Palisse volcanics, French Massif Central. *Geophysical Journal International*, *193*(2), 585–602. doi: 10.1093/gji/ggs115

Boness, N. L., & Zoback, M. D. (2006). Mapping stress and structurally controlled crustal shear velocity anisotropy in California. *Geology*, *34*(10). doi: 10.1130/G22309.1

Carlson, R. L., & Herrick, C. N. (1990). Densities and porosities in the oceanic crust and their variations with depth and age. *Journal of Geophysical Research*, *95*(B6), 9153–9170. doi: 10.1029/JB095iB06p09153

Christensen, N. I. (1984). Pore pressure and oceanic crustal seismic structure. *Geophysical Journal International*, *79*(2), 411–423. doi: 10.1111/j.1365-246X.1984.tb02232.x

Crampin, S. (1984). An introduction to wave propagation in anisotropic media. *Geophysical Journal of the Royal Astronomical Society*, *76*(1), 17–28. doi: 10.1111/j.1365-246X.1984.tb05018.x

Crampin, S. (1994). The fracture criticality of crustal rocks. *Geophysical Journal International*, *118*(2), 428–438. doi: 10.1111/j.1365-246X.1994.tb03974.x

Darbyshire, F. A., White, R. S., & Priestley, K. F. (2000). Structure of the crust and uppermost mantle of Iceland from a combined seismic and gravity study. *Earth and Planetary Science Letters*, *181*(3), 409–428. doi: 10.1016/S0012-821X(00)00206-5

Davis, J. C., & Sampson, R. J. (1973). *Statistics and data analysis in geology* (Vol. 646). Wiley New York.

de Lorenzo, S., & Trabace, M. (2011). Seismic anisotropy of the shallow crust in the Umbria–Marche (Italy) region. *Physics of the Earth and Planetary Interiors*, *189*(1-2), 34–46. doi: 10.1016/j.pepi.2011.09.008

de Zeeuw-van Dalfsen, E., Pedersen, R., Hooper, A., & Sigmundsson, F. (2012). Subsidence of Askja caldera 2000-2009: Modelling of deformation processes at an extensional plate boundary, constrained by time series InSAR analysis. *Journal of Volcanology and Geothermal Research*, *213-214*, 72–82. doi: 10.1016/j.jvolgeores.2011.11.004

de Zeeuw-van Dalfsen, E., Rymer, H., Sturkell, E., Pedersen, R., Hooper, A., Sigmundsson, F., & Ófeigsson, B. (2013). Geodetic data shed light on ongoing caldera subsidence at Askja, Iceland. *Bulletin of volcanology*, *75*(5), 1–13. doi: 10.1007/s00445-013-0709-2

Donaldson, C., Winder, T., Caudron, C., & White, R. S. (2019). Crustal seismic velocity responds to a magmatic intrusion and seasonal loading in Iceland's Northern Volcanic Zone. *Science Advances*, *5*(11), eaax6642. doi: 10.1126/sciadv.aax6642

Drew, J., White, R. S., Tilmann, F., & Tarasewicz, J. (2013). Coalescence microseismic mapping. *Geophysical Journal International*, *195*(3), 1773–1785. doi: 10.1093/gji/ggt331

Drouin, V., Sigmundsson, F., Ófeigsson, B. G., Hreinsdóttir, S., Sturkell, E., & Einarsson, P. (2017). Deformation in the Northern Volcanic Zone of Iceland 2008–2014: An interplay of tectonic, magmatic, and glacial isostatic deformation. *Journal of Geophysical Research: Solid Earth*, *122*(4), 3158–3178. doi: 10.1002/2016JB013206

Einarsson, P. (1991). Earthquakes and present-day tectonism in Iceland. *Tectonophysics*, *189*(1-4), 261–279. doi: 10.1016/0040-1951(91)90501-I

Garcia, S., Arnaud, N. O., Angelier, J., Bergerat, F., & Homberg, C. (2003). Rift jump process in Northern Iceland since 10 Ma from 40Ar/ 39Ar geochronology. *Earth and Planetary Science Letters*, *214*(3-4), 529–544. doi: 10.1016/S0012-821X(03)00400-X

Graettinger, A. H., McGarvie, D. W., Skilling, I. P., Höskuldsson, A. H., & Strand, K. (2019). Ice-confined construction of a large basaltic volcano—Austurfjöll massif, Askja, Iceland. *Bulletin of Volcanology*, *81*(2). doi: 10.1007/s00445-019-1269-x

Green, R. G., White, R. S., & Greenfield, T. (2014). Motion in the north Iceland volcanic rift zone accommodated by bookshelf faulting. *Nature Geoscience*, *7*(1), 29–33. doi: 10.1038/ngeo2012

Greenfield, T., White, R. S., & Roecker, S. (2016). The magmatic plumbing system of the Askja central volcano, Iceland, as imaged by seismic tomography. *Journal of Geophysical Research: Solid Earth*, *121*(10), 7211–7229. doi: 10.1002/2016JB013163

Greenfield, T., White, R. S., Winder, T., & Ágústsdóttir, T. (2018). Seismicity of the Askja and Bárðarbunga volcanic systems of Iceland, 2009–2015. *Journal of Volcanology and Geothermal Research*, *391*. doi: 10.1016/j.jvolgeores.2018.08.010

Hammond, J. O., Kendall, J.-M., Wookey, J., Stuart, G., Keir, D., & Ayele, A. (2014). Differentiating flow, melt, or fossil seismic anisotropy beneath Ethiopia. *Geochemistry, Geophysics, Geosystems*, *15*(5), 1878–1894. doi: 10.1002/2013GC005185

Han, S.-C., Schmerr, N., Neumann, G., & Holmes, S. (2014). Global characteristics of porosity and density stratification within the lunar crust from GRAIL gravity and Lunar Orbiter Laser Altimeter topography data. *Geophysical Research Letters*, *41*(6), 1882–1889. doi: 10.1002/2014GL059378

Harris, C. R., Millman, K. J., van der Walt, S. J., Gommers, R., Virtanen, P., Cournapeau, D., … others (2020). Array programming with NumPy. *Nature*, *585*(7825), 357–362.

Heimisson, E. R., & Segall, P. (2020). Physically Consistent Modeling of Dike-Induced Deformation and Seismicity: Application to the 2014 Bárðarbunga Dike, Iceland. *Journal of Geophysical Research: Solid Earth*, *125*(2), 1–21. doi: 10.1029/2019JB018141

Hjartardóttir, A. R., Einarsson, P., Magnúsdóttir, S., Björnsdóttir, T., & Brandsdóttir, B. (2016). Fracture systems of the Northern Volcanic Rift Zone, Iceland: An onshore part of the Mid-Atlantic plate boundary. In *Geological society special publication.* doi: 10.1144/SP420.1

Holtzman, B. K., Kohlstedt, D. L., Zimmerman, M. E., Heidelbach, F., Hiraga, T., & Hustoft, J. (2003). Melt segregation and strain partitioning: Implications for seismic anisotropy and mantle flow. *Science*, *301*(5637), 1227–1230. doi: 10.1126/science.1087132

Hunter, J. D. (2007). Matplotlib: A 2D graphics environment. *Computing in Science & Engineering*, *9*(3), 90–95. doi: 10.1109/MCSE.2007.55

Illsley-Kemp, F., Greenfield, T., & Keir, D. (2018). Seismic Anisotropy Reveals a Dynamic Link Between Adjacent Magmatic Segments Prior to Dyke Intrusion. *Journal of Geophysical Research: Solid Earth*, *123*(11), 9800–9816. doi: 10.1029/2018JB016420

Illsley-Kemp, F., Savage, M. K., Keir, D., Hirschberg, H. P., Bull, J. M., Gernon,

T. M., . . . Goitom, B. (2017). Extension and stress during continental breakup: Seismic anisotropy of the crust in Northern Afar. *Earth and Planetary Science Letters*, *477*, 41–51.

Illsley-Kemp, F., Savage, M. K., Wilson, C. J., & Bannister, S. (2019). Mapping stress and structure from subducting slab to magmatic rift: crustal seismic anisotropy of the North Island, New Zealand. *Geochemistry, Geophysics, Geosystems*, *20*(11), 5038–5056.

Johnson, J. H., Savage, M. K., & Townend, J. (2011). Distinguishing between stress-induced and structural anisotropy at Mount Ruapehu volcano, New Zealand. *Journal of Geophysical Research: Solid Earth*, *116*(12), 1–18. doi: 10.1029/2011JB008308

Keir, D., Kendall, J. M., Ebinger, C. J., & Stuart, G. W. (2005). Variations in late syn-rift melt alignment inferred from shear-wave splitting in crustal earthquakes beneath the Ethiopian rift. *Geophysical Research Letters*, *32*(23), 1–4. doi: 10.1029/2005GL024150

Kendall, J.-M., Stuart, G., Ebinger, C., Bastow, I., & Keir, D. (2005). Magma-assisted rifting in Ethiopia. *Nature*, *433*(7022), 146–148. doi: 10.1038/nature03161

LaFemina, P. C., Dixon, T. H., Malservisi, R., Árnadóttir, T., Sturkell, E., Sigmundsson, F., & Einarsson, P. (2005). Geodetic GPS measurements in south Iceland: Strain accumulation and partitioning in a propagating ridge system. *Journal of Geophysical Research: Solid Earth*, *110*(B11). doi: 10.1029/2005JB003675

Lesage, P., Heap, M. J., & Kushnir, A. (2018). A generic model for the shallow velocity structure of volcanoes. *Journal of Volcanology and Geothermal Research*, *356*, 114–126.

Lomax, A., Virieux, J., Volant, P., & Berge-Thierry, C. (2000). Probabilistic Earthquake Location in 3D and Layered Models.. doi: 10.1007/978-94-015-9536-0_5

Lund, B., & Townend, J. (2007). Calculating horizontal stress orientations with full or partial knowledge of the tectonic stress tensor. *Geophysical Journal International*, *170*(3), 1328–1335.

Maclennan, J., Mckenzie, D., & Gronvold, K. (2001). Plume-driven upwelling under Central Iceland. *Earth and Planetary Science Letters*, *194*(1-2), 67–82. doi: 10.1016/S0012-821X(01)00553-2

Martens, H. R., & White, R. S. (2013). Triggering of microearthquakes in Iceland by volatiles released from a dyke intrusion. *Geophysical Journal International*, *194*(3), 1738–1754. doi: 10.1093/gji/ggt184

Menke, W., Brandsdottir, B., Jakobsdottir, S., & Stefansson, R. (1994). Seismic anisotropy in the crust at the mid-Atlantic plate boundary in south-west Iceland. *Geophysical Journal International*, *119*(3), 783–790.

Mitchell, M. A., White, R. S., Roecker, S., & Greenfield, T. (2013). Tomographic image of melt storage beneath Askja Volcano, Iceland using local microseismicity. *Geophysical Research Letters*, *40*(19), 5040–5046. doi: 10.1002/grl.50899

Nowacki, A., Wilks, M., Kendall, J. M., Biggs, J., & Ayele, A. (2018). Characterising hydrothermal fluid pathways beneath Aluto volcano, Main Ethiopian Rift, using shear wave splitting. *Journal of Volcanology and Geothermal Research*, *356*, 331–341. doi: 10.1016/j.jvolgeores.2018.03.023

Nuttli, O. (1961). The effect of the earth's surface on the S wave particle motion. *Bulletin of the Seismological Society of America*, *51*(2), 237–246.

Okada, Y. (1992). Internal deformation due to shear and tensile faults in a half-space. *Bulletin of the Seismological Society of America*, *82*(2), 1018–1040.

Pagli, C., Sigmundsson, F., Árnadóttir, T., Einarsson, P., & Sturkell, E. (2006). Deflation of the Askja volcanic system: Constraints on the deformation source from combined inversion of satellite radar interferograms and GPS measurements. *Journal of Volcanology and Geothermal Research*, *152*(1-2), 97–108. doi: 10.1016/j.jvolgeores.2005.09.014

pandas development team, T. (2021). *pandas-dev/pandas: Pandas 1.3.0rc1.* Zenodo. doi: 10.5281/zenodo.4940217

Pedersen, R., Sigmundsson, F., & Masterlark, T. (2009). Rheologic controls on inter-rifting deformation of the Northern Volcanic Zone, Iceland. *Earth and Planetary Science Letters*, *281*(1-2), 14–26. doi: 10.1016/j.epsl.2009.02.003

Savage, M. K., Wessel, A., Teanby, N. A., & Hurst, A. W. (2010). Automatic measurement of shear wave splitting and applications to time varying anisotropy at Mount Ruapehu volcano, New Zealand. *Journal of Geophysical Research: Solid Earth*, *115*(12), 1–17. doi: 10.1029/2010JB007722

Sigmundsson, F., Hooper, A., Hreinsdóttir, S., Vogfjörd, K. S., Ófeigsson, B. G., Heimisson, E. R., … Eibl, E. P. (2014). Segmented lateral dyke growth in a rifting event at Bárðarbunga volcanic system, Iceland. *Nature*, *517*(7533). doi: 10.1038/nature14111

Silver, P. G., & Chan, W. W. (1991). Shear wave splitting and subcontinental mantle deformation. *Journal of Geophysical Research: Solid Earth*, *96*(B10), 16429–16454. doi: 10.1029/91JB00899

Soosalu, H., Key, J., White, R. S., Knox, C., Einarsson, P., & Jakobsdóttir, S. S.

(2010). Lower-crustal earthquakes caused by magma movement beneath Askja volcano on the north Iceland rift. *Bulletin of Volcanology*, *72*(1), 55–62. doi: 10.1007/s00445-009-0297-3

Sturkell, E., Sigmundsson, F., & Slunga, R. (2006). 1983-2003 decaying rate of deflation at Askja caldera: Pressure decrease in an extensive magma plumbing system at a spreading plate boundary. *Bulletin of Volcanology*, *68*(7-8), 727–735. doi: 10.1007/s00445-005-0046-1

Teanby, N. A., Kendall, J. M., & van der Baan, M. (2004). Automation of shear-wave splitting measurements using cluster analysis. *Bulletin of the Seismological Society of America*, *94*(2), 453–463. doi: 10.1785/0120030123

Thomas, C., & Kendall, J. (2002). The lowermost mantle beneath northern Asia—II. Evidence for lower-mantle anisotropy. *Geophysical Journal International*, *151*(1), 296–308. doi: 10.1046/j.1365-246X.2002.01760.x

Toda, S., Stein, R., Sevilgen, V., & Lin, J. (2011). *Coulomb 3.3 Graphic-rich deformation and stress-change software for earthquake, tectonic, and volcano research and teaching-user guide.* (Tech. Rep.).

Tryggvason, E. (1989). Ground deformation in Askja, Iceland: Its source and possible relation to flow of the mantle plume. *Journal of Volcanology and Geothermal Research*, *39*(1), 61–71. doi: 10.1016/0377-0273(89)90021-8

Virtanen, P., Gommers, R., Oliphant, T. E., Haberland, M., Reddy, T., Cournapeau, D., … others (2020). SciPy 1.0: fundamental algorithms for scientific computing in Python. *Nature methods*, *17*(3), 261–272.

Volk, O., White, R. S., Pilia, S., Green, R. G., Maclennan, J., & Rawlinson, N. (2021). Oceanic crustal flow in Iceland observed using seismic anisotropy. *Nature Geoscience*, *14*(3), 168–173. doi: 10.1038/s41561-021-00702-7

Walsh, E., Arnold, R., & Savage, M. K. (2013). Silver and Chan revisited. *Journal of Geophysical Research: Solid Earth*, *118*(10), 5500–5515. doi: 10.1002/jgrb.50386

Wang, X. Q., Schubnel, A., Fortin, J., David, E. C., Guéguen, Y., & Ge, H. K. (2012). High Vp/Vs ratio: Saturated cracks or anisotropy effects? *Geophysical Research Letters*, *39*(11), 2–7. doi: 10.1029/2012GL051742

Wessel, P., Luis, J., Uieda, L., Scharroo, R., Wobbe, F., Smith, W., & Tian, D. (2019). The Generic Mapping Tools version 6. *Geochemistry, Geophysics, Geosystems*, *20*(11), 5556–5564. doi: 10.1029/2019GC008515

White, R. S., & McKenzie, D. (1995). Mantle plumes and flood basalts. *Journal of Geophysical Research: Solid Earth*, *100*(B9), 17543–17585. doi: 10.1029/95jb01585

Winder, T., White, R. S., Green, R. G., & Greenfield, T. (2018). A Surge in Seismicity in a Network of Cross-Cutting Conjugate Strike-Slip Faults Triggered by the 2014 Bárðarbunga-Holuhraun Dike Intrusion. In *Agu fall meeting abstracts* (Vol. 2018, pp. V23C–08).

Supporting Information for "On the origin of seismic anisotropy in the shallow crust of the Northern Volcanic Zone, Iceland"

C. A. Bacon[1], J. Johnson[2], R. S. White[1], N. Rawlinson[1]

[1]Department of Earth Sciences, University of Cambridge, UK

[2]School of Environmental Sciences, University of East Anglia, UK

Contents of this file

Introduction

This supporting document contains some additional examples of shear-wave splitting measurements and the results of the parameter trials used for the regridding of shear-wave splitting results as outlined in Sections 3.2.1 and 3.2.2. In addition, there is a table that provides the parameters used by MFAST and the captions for datasets S1 and S2, which can be downloaded separately.

Data Set S1. The input file used for the Coulomb stress modeling outlined in Section 4.2.

Data Set S2. The result file containing all of the splitting measurements used in this study.

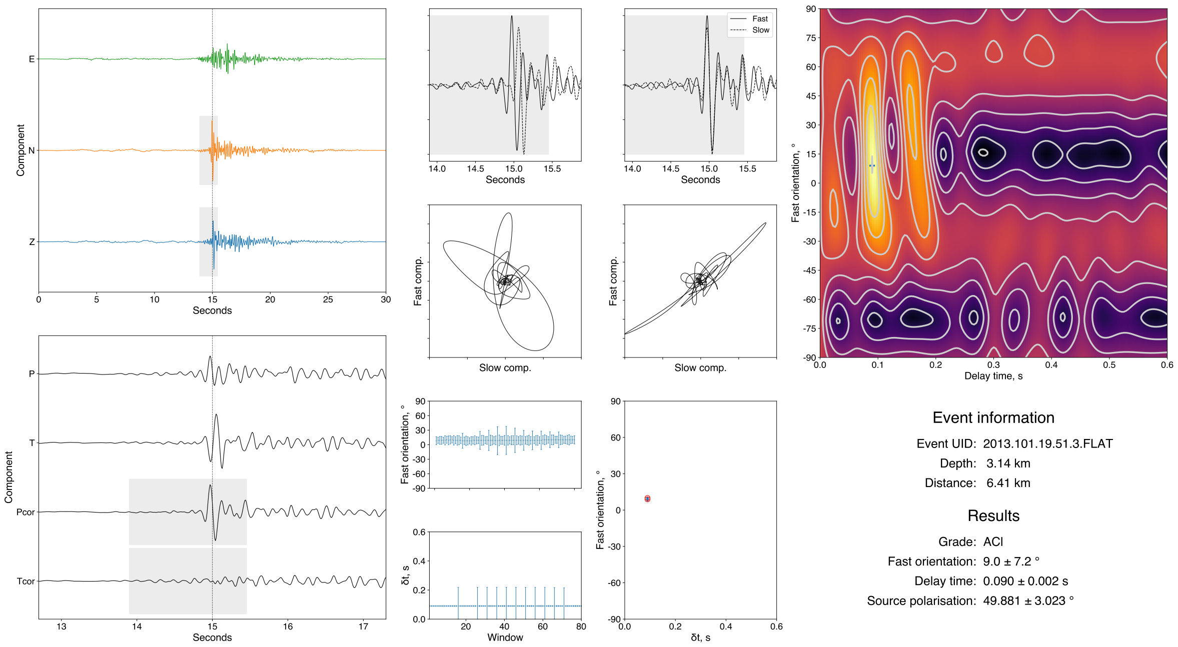

Figure S1. Example of a good splitting measurement at FLAT for a repeating earthquake (multiplet)—see Figure S2. (a) shows the raw data for the East (green), North (orange), and Vertical (blue) components. (b) shows a zoom in around the S phase arrival rotated onto the nominal 'radial' (P) and 'transverse' (T) axes before and after correction for splitting. Panels (c) and (d) show the phase arrivals rotated onto the 'fast' and 'slow' axes before and after correction, with (e) and (f) showing the corresponding particle motion. There is a clear linearisation of the particle motion of the horizontal components and removal of energy from the transverse component. Panels (g) - (i) show the results of the multiple window trials and the cluster analysis. Finally, (j) shows the resultant grid of the minimised eigenvalue. The blue cross denotes the optimal (δt, ϕ) pair.

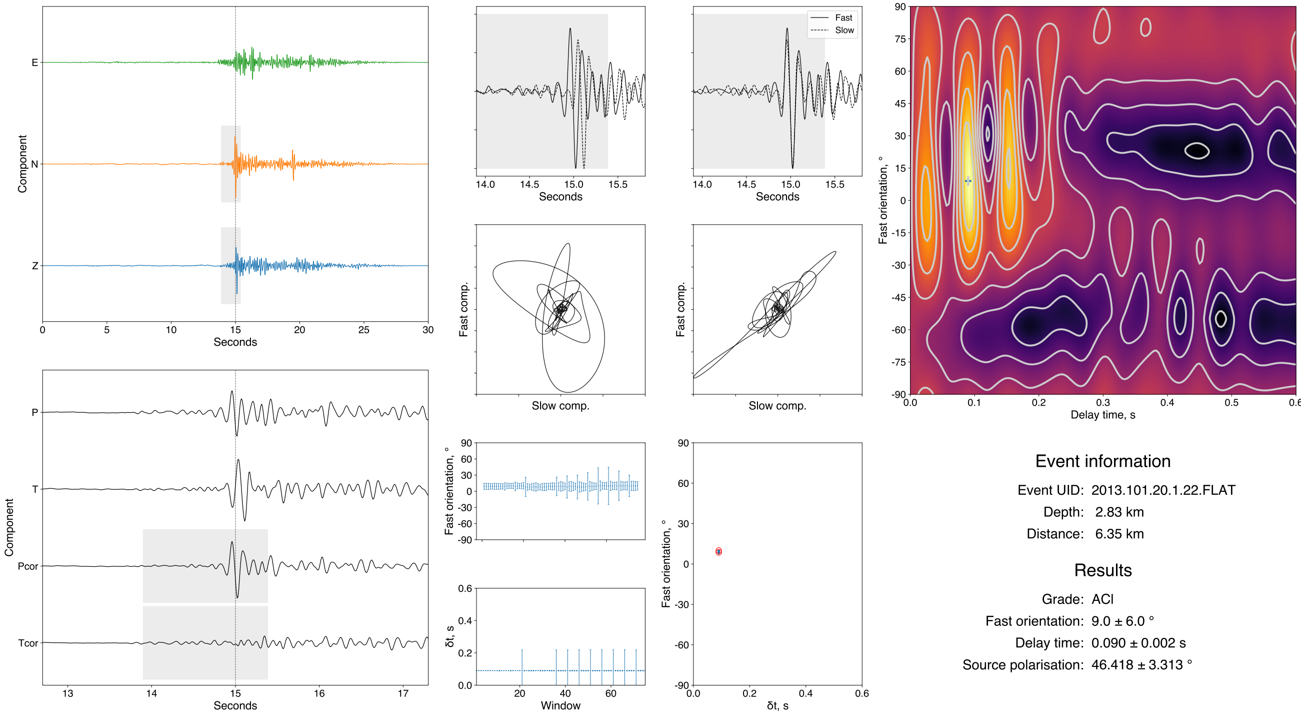

Figure S2. Example of a good splitting measurement at FLAT for a repeating earthquake (multiplet)—see Figure S1. Panels the same as Figure S1.

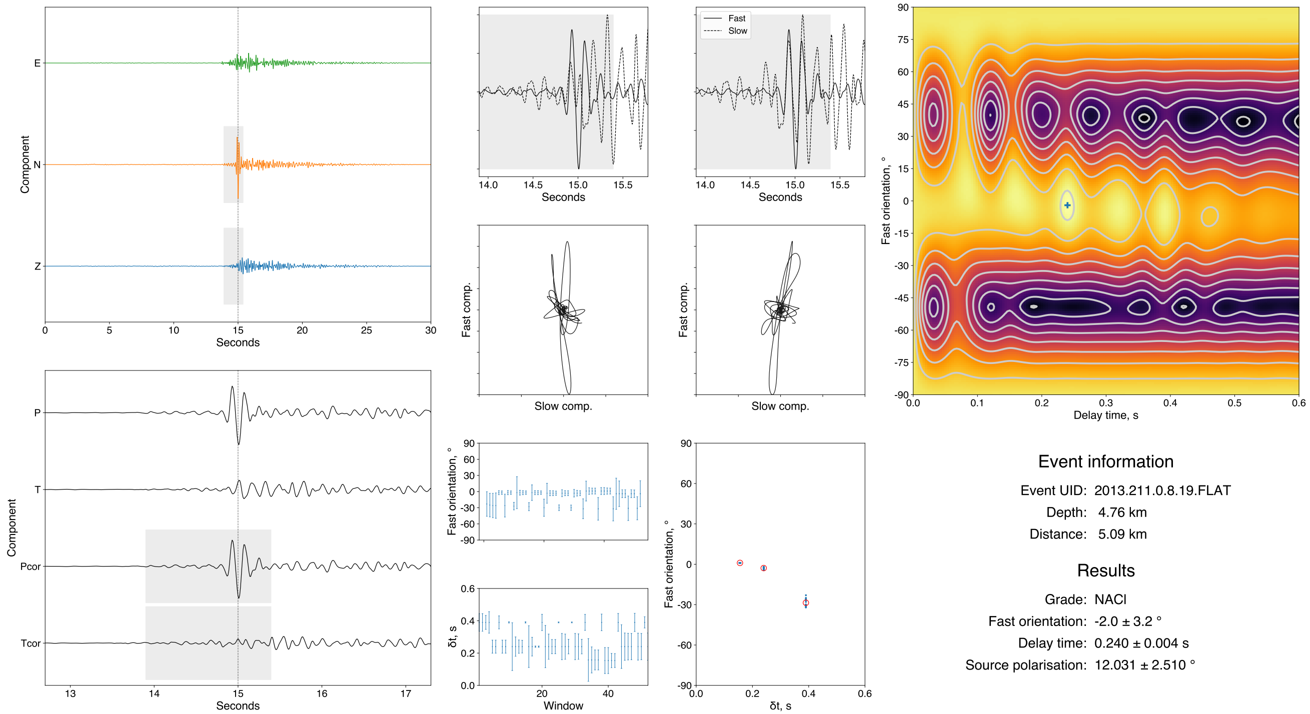

Figure S3. Example of a null splitting measurement at FLAT. Panels the same as Figure S1.

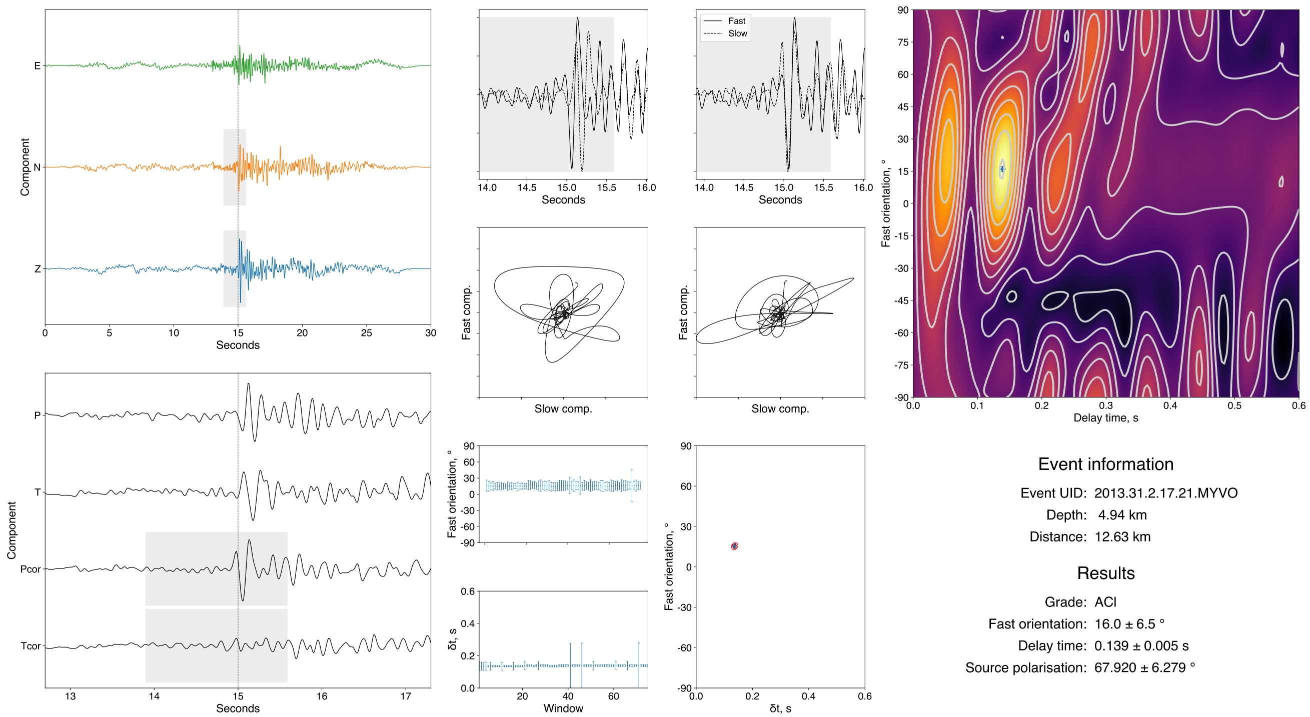

Figure S4. Example of a good splitting measurement at MYVO. Panels the same as Figure S1.

Parameter name	Description	Value
nwbeg	Number of measurement window start times tested	5
nwend	Number of measurement window end times tested	16
dt_beg	Time step size between window start times	0.2
dt_end	Time step size between window end times	0.0158276
dtlag_max	Maximum allowable error in tlag for inclusion in clustering	0.144823
dfast_max	Maximum allowable error in fast for inclusion in clustering	40
t_off_beg	First time of start window	0.3
t_off_end	First time of end window	0.279293
tlag_scale	Maximum time lag	0.579293
fast_scale	Maximum fast direction	180
max_no_clusters	Maximum number of clusters to test during cluster analysis	15
nmin	Minimum number of points in an acceptable cluster	5

Table S1. Table giving the MFAST parameter values used for this study.

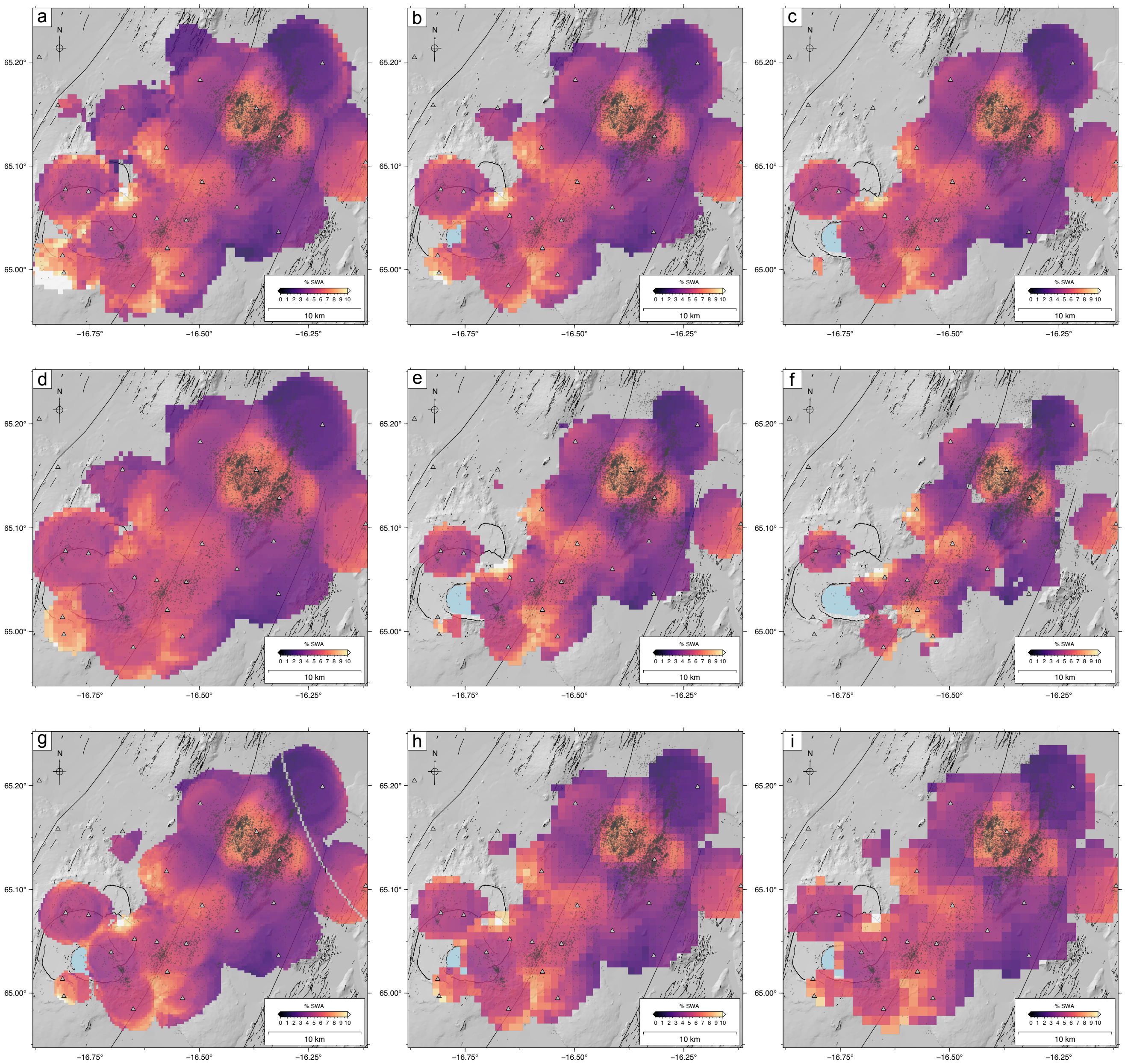

Figure S5. Shear wave anisotropy (SWA) re-gridding parameter trials. Each row shows a different parameter variation: a–c show variations in the minimum number of observations required per cell, with values of 3, 8, and 15 from left to right; d–f show variations in the width of the Gaussian kernel used for smoothing the data, with values of 1500, 2000, and 3500 from left to right; g–i show variations in the grid cell size with values of 0.25 x 0.25 km^2, 0.75 x 0.75 km^2, and 1 x 1 km^2 from left to right. There are no notable differences between the trials, suggesting that the features observed are robust.

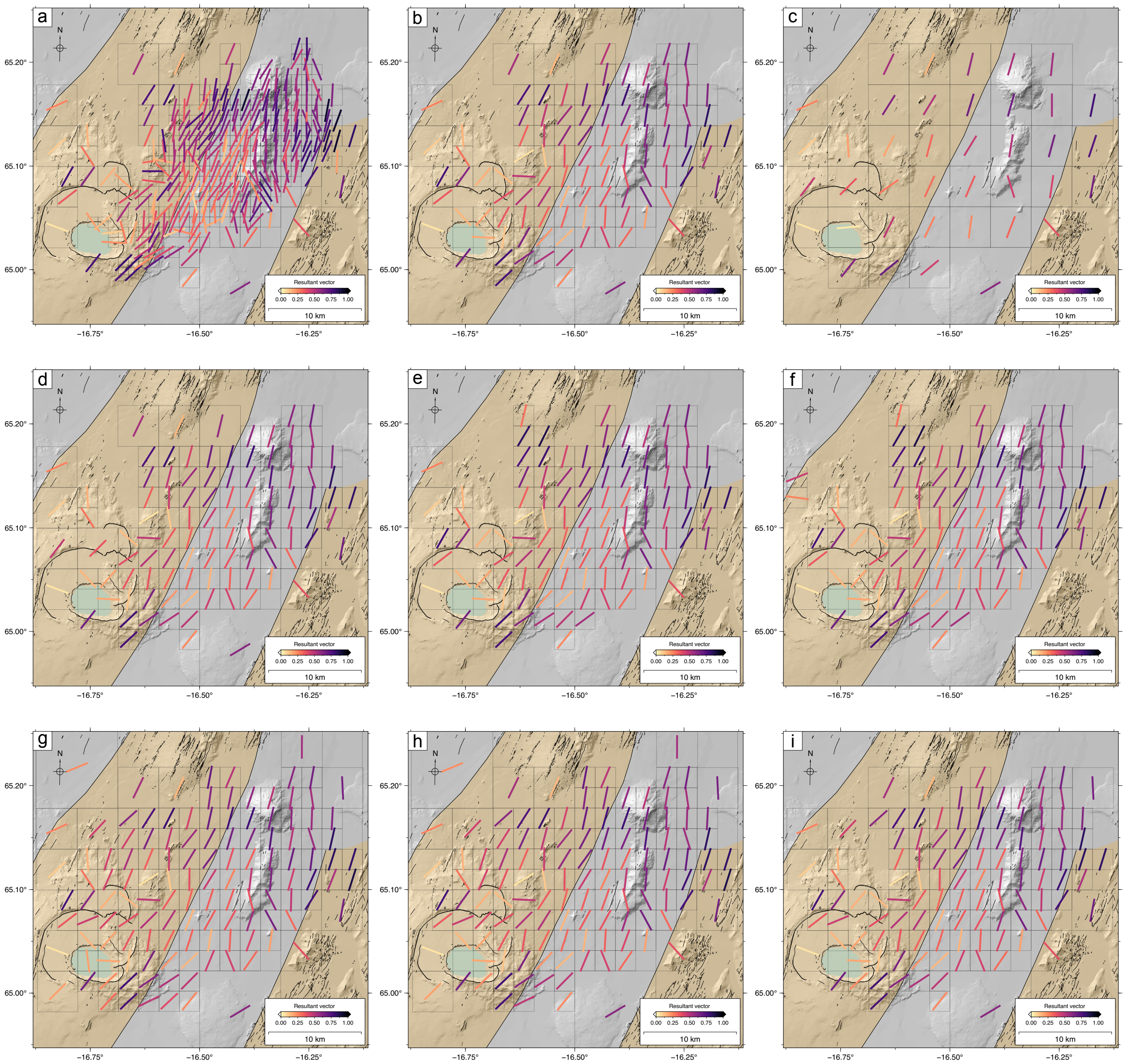

Figure S6. Fast polarization (ϕ) re-gridding parameter trials. Each row shows a different parameter variation: a–c show variations in the minimum cell size, with values of 1 x 1 km^2, 1.5 x 1.5 km^2, and 3 x 3 km^2 from left to right; d–f show variations in the maximum number of observations before a cell is subdivided, *n_max*, with values of 100, 150, and 250 from left to right; g–i show variations in the minimum number of observations required for a cell to be retained, *n_min*, with values of 20, 30, and 50 from left to right. There are no notable differences between the trials, suggesting that the features observed are robust.

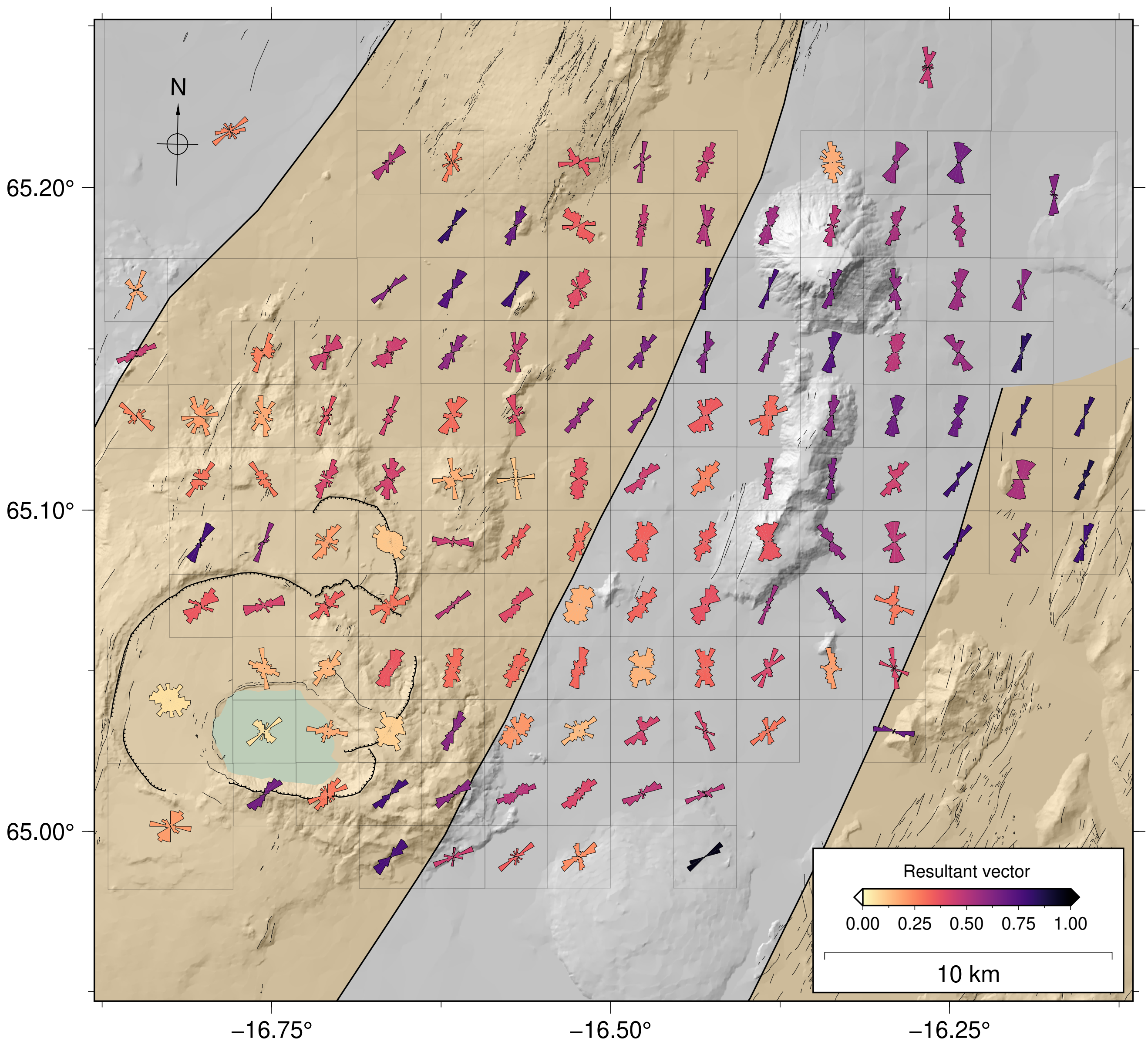

Figure S7. Lateral variations in observed fast axis orientations, ϕ. The observations have been assigned to the midpoint between source and receiver, then re-gridded using a quadtree method. The resultant grid is plotted using faint black lines. Within each cell, the rose diagram shows the distribution of fast axis orientation measurements, colored by the 'resultant vector' which is a measure of dispersion/coherence of the orientation data. Darker colors indicate stronger coherence.